Journal of Magnetism and Magnetic Materials 560 (2022) 169660

Contents lists available at ScienceDirect

Journal of Magnetism and Magnetic Materials

journal homepage: www.elsevier.com/locate/jmmm

Anisotropic magnetoresistance (AMR) of cobalt: hcp-Co vs. fcc-Co

M. El-Tahawy [a,b,c], L. Péter [a], L.F. Kiss [a], J. Gubicza [b], Zs. Czigány [d], G. Molnár [d], I. Bakonyi [a,*]

[a] Institute for Solid State Physics and Optics, Wigner Research Centre for Physics. H–1121 Budapest, Konkoly-Thege út 29-33, Hungary
[b] Department of Materials Physics, Eötvös Loránd University, H-1117 Budapest, Pázmány Péter sétány 1/A, Hungary
[c] Physics Department, Faculty of Science, Tanta University, 31527 Tanta, Egypt
[d] Institute for Technical Physics and Materials Science, Centre for Energy Research, H–1121 Budapest, Konkoly-Thege út 29-33, Hungary

ARTICLE INFO

Keywords:
Anisotropic magnetoresistance (AMR)
Magnetic properties
hcp-Co
fcc-Co

ABSTRACT

In spite of the numerous works devoted to studying the magnetoresistance of Co metal, very diverging results have been reported in the literature on the magnitude of the anisotropic magnetoresistance (AMR) ratio of Co samples mostly without detailed structural characterization. Therefore, the main purpose of the present work was to establish if the crystal structure of Co has an effect on the AMR ratio. With the help of structural studies by X-ray diffraction (XRD) and transmission electron microscopy, fully hcp-Co and predominantly fcc–Co polycrystalline foils were produced by electrodeposition and their magnetoresistance curves MR(H) were measured at room temperature in magnetic fields up to $H = 8$ kOe. The MR(H) curves indicated much lower saturation fields for fcc-Co than for hcp-Co, in good agreement with the significantly larger magnetocrystalline anisotropy of the hcp phase. These findings were supported also by the measured magnetization isotherms. The coercive field and MR(H) peak position data indicated a magnetically softer behavior of the fcc-Co phase than that of the hcp-Co phase, in agreement with literature findings. Finally, it was established that the AMR ratio is about +1.2 % for hcp-Co whereas it is about +1.9 % for the predominantly fcc-Co samples. By having an estimated volume fraction of the hcp-Co phase in the latter samples from the XRD studies, we could assess an AMR ratio of about 2.2 % for pure fcc-Co. It is the first time that the AMR ratio has been determined separately for the two crystalline phases of Co and the finding that AMR(fcc–Co) ≈ 1.8 AMR(hcp-Co) is a hitherto unknown result. Finally, our AMR results for the two phases of Co metal are discussed in the light of recent progress on the microscopic mechanisms of the AMR effect.

1. Introduction

In the late 1850s, Thomson [1,2] discovered that the electrical resistance of Fe and Ni metals increases in a magnetic field H oriented parallel to the measuring current (longitudinal effect) and decreases when H is perpendicular to the current direction (transverse effect). Numerous studies [3–44] have later demonstrated similar resistance changes also in Co metal when placed in a magnetic field and the resistance change for Co was found to be larger than for Fe, but smaller than for Ni. Most of the magnetoresistance (MR) measurements on Co metal have been carried out on polycrystalline samples except for a few studies performed on single crystals of hcp-Co [18,40–44]. These latter studies mainly aimed at exploring the Fermi surface properties of Co metal, but their results will not be discussed here since from our polycrystalline Co samples such kind of information can be derived only in a limited manner for the Fermi surface properties due to the averaging of the Fermi surfaces of the randomly oriented crystallites.

The field dependence of the resistance in the longitudinal and transverse configurations (the so-called longitudinal and transverse magnetoresistance, LMR and TMR, respectively) has been extensively studied in all three ferromagnetic metals (Fe, Co and Ni) and their alloys in polycrystalline form and these results are properly discussed in Refs. 22 and 45–47. The direction of the field-induced resistance changes (LMR > 0 and TMR < 0) as measured for the pure ferromagnetic metals is the same for most ferromagnetic alloys as well. This implies an anisotropy of the resistivity in metallic ferromagnets and this is called an anisotropic magnetoresistance (AMR) effect (often termed also as spontaneous or ferromagnetic resistivity anisotropy) [22,45–47].

The magnitude of the AMR effect is defined [46–50] as the difference $\rho_{Ls} - \rho_{Ts}$ where the resistivities ρ_{Ls} and ρ_{Ts} are the zero-field values of the resistivities of the magnetically saturated (monodomain) state in the longitudinal and transverse configurations, respectively. The subscript s

* Corresponding author.
E-mail address: bakonyi.imre@wigner.hu (I. Bakonyi).

https://doi.org/10.1016/j.jmmm.2022.169660
Received 17 February 2022; Received in revised form 17 June 2022; Accepted 25 June 2022
Available online 30 June 2022

refers to the fact that the zero-field resistivities can only be obtained by extrapolating the measured $\rho_L(H)$ and $\rho_T(H)$ values to $H = 0$ from the magnetically saturated (monodomain) regions at high fields. It should be noted that in an exact treatment, the extrapolation should be made to zero induction B [46,49]. However, at not too low temperatures such as, e.g., at room temperature, there is only a negligible difference in the resistivity values obtained for $H \rightarrow 0$ and for $B \rightarrow 0$ [51,52].

The quantity $\Delta\rho_{AMR} = \rho_{Ls} - \rho_{Ts}$ can be called as the resistivity anisotropy splitting [50]. By defining the isotropic resistivity as $\rho_{is} = (\rho_{Ls} + 2\rho_{Ts})/3$ [22,46,49], the AMR ratio is obtained as $\Delta\rho_{AMR}/\rho_{is}$.

Since ferromagnetic metals and alloys play an important role as electrodes in spintronic devices, the AMR value is an important parameter concerning their spin transport characteristics. This explains well the renewed experimental and theoretical interest in studying the AMR and related magnetotransport phenomena of ferromagnetic metals and alloys in the recent decade [36–39,48,50,52–62], especially from the viewpoint of distinguishing between the extrinsic and intrinsic contributions to the magnetotransport parameters.

When looking at specifically the results of the numerous studies on the field dependence of the resistivity of polycrystalline Co metal [3–39], we can see a very large scatter of the reported AMR values for various reasons. Even if the field dependence of the resistivity was measured in both the LMR and TMR configurations, in many cases the applied field was not sufficient to reach saturation and the Co samples were not always properly characterized for purity or were not sufficiently pure.

Another complication arises from the often lacking information about the crystal structure of the Co specimens investigated. The stable phase of pure Co metal exhibits the hexagonal close-packed (hcp) structure at room temperature and at $T = 695$ K, hcp-Co transforms to a face-centered cubic (fcc) phase [63]. Since the packing density (or atomic volume) of hcp-Co and fcc-Co differs only negligibly [64] and the energy difference between the two phases is also very small [65], the formation of fcc crystals of Co is highly probable and fcc-Co can exist as a metastable phase even at room temperature. For the preparation of Co samples for magnetoresistance measurements, the Co ingot was often annealed above the hcp ↔ fcc transformation temperature to get a stress-free state. However, if the ingot was then cooled to room temperature too fast, i.e., through non-equilibrium states, some fcc fraction may have been retained at room temperature. It has also been a common way, for the convenience of being able to accurately measure small resistance changes in a magnetic field, to prepare thin film or foil samples via atom-by-atom deposition methods (evaporation, sputtering, and electrodeposition). These latter are non-equilibrium techniques which may promote the formation of the metastable fcc-Co phase. Therefore, the Co thin film or foil samples for which the AMR was studied may have contained various fractions of hcp-Co and fcc-Co crystals. If the two structural modifications of Co exhibit different AMR ratios, this can be also a reason for the observed scatter of the AMR data reported for Co metal.

In view of the above discussion, the crystal structure identification of the Co samples is of great importance, but no structural studies have been reported in most of the works. However, even if one carries out an X-ray diffraction (XRD) study of a Co sample, special care should be exercised. The reason for this is that according to the ASTM Powder Diffraction Files of the hcp–Co [66] and fcc-Co [67] phases, besides the unique Bragg reflections characteristic of the hcp and fcc phase only [hcp-Co:$(10\bar{1}0)$,$(10\bar{1}1)$,$(10\bar{1}2)$,$(10\bar{1}3)$,$(20\bar{2}0)$, $(20\bar{2}1)$ and (0004); fcc–Co: (200) and (222)], there are three closely coinciding reflection pairs of the two crystal structures: hcp(0002)/fcc(111), hcp$(11\bar{2}0)$/fcc(220) and hcp$(11\bar{2}2)$/fcc(311). When using $CoK_{\alpha 1}$ radiation for an XRD study in the usual $\theta - 2\theta$ geometry, the differences in the 2θ positions of the hcp/fcc coinciding peaks are 0.320 deg, 0.065 deg and 0.352 deg, respectively, for the above mentioned coinciding peak pairs. These differences are so small that in a conventional XRD pattern usually no distinction can be made whether the observed reflection peak belongs to the hcp or fcc phase, especially for small crystallite sizes inducing a strong broadening of the XRD lines. In addition, in the case of a crystallographic texture, the lack of unique peaks of a phase does not mean unequivocally the absence of that phase. For instance, in fcc films prepared, e.g., by electrodeposition [68] or sputtering [69], (111) and (220) textures are often formed. For cobalt specifically, both the fcc (111) and fcc(220) peaks are coincident peaks with hcp-Co reflections; therefore, such a textured fcc-Co phase may exist even if apparently hcp peaks are only observed in the conventional XRD patterns taken with $\theta - 2\theta$ reflection geometry. Therefore, various XRD measurement geometries and transmission electron microscopy (TEM) selected area electron diffraction (SAED) patterns can further help in a possible assignment of the observed coinciding Bragg reflections to one of the hcp and fcc phases.

By reviewing the papers on the MR study of Co metal, we can see that in several cases electrodeposition was used to prepare samples which are very appropriate for MR measurements since either relatively thin foils and films [5–8,30,31,38] or nanowires [27,29,32,37] can be produced and the limited sample dimensions ensure a high resistance. Furthermore, already as early as a century ago, it was revealed that electrodeposited Co metal may contain comparable amounts of both the hcp and the fcc phases [70]. It turned out later from the extensive experimental work devoted to this topic (see, e.g., Ref. 71 and references therein) that the electrodeposition conditions strongly influence the ratio of the two structural modifications in the Co deposit. The general consensus emerging from these investigations [71] is that a high *pH* (about 5) and a low deposition current density (e.g., 5 mA/cm^2) favor the formation of the stable hcp-Co phase. On the other hand, a bath with low *pH* (between about 2 to 3) and a high deposition current density (e.g., 150 mA/cm^2) promote the formation of the fcc-Co phase. (It should be kept, however, in mind that these mentioned preferential effects refer to baths of about 1 mol/liter Co^{2+} concentration, while the trend may be somewhat different for more dilute solutions, especially concerning the appropriate current density values). Since at high current densities strong hydrogen evolution at the cathode accompanies the Co deposition (yielding a current efficiency even as low as 30 %), it is usually assumed that the formation of the fcc-Co crystals is probably induced by the presence of hydrogen. Although some hydrogen may be temporarily dissolved in the lattice of the deposited Co layer, since the solubility of H in Co is extremely low under ambient conditions, the hydrogen is certainly quickly released from the Co lattice after deposition. Therefore, once the fcc lattice is formed, hydrogen does not contribute anymore either to the room-temperature persistence of fcc-Co or to its resistivity measured a sufficiently long time after the deposition.

In view of the above considerations, it was aimed in the present study to produce single-phase hcp-Co and fcc-Co polycrystalline samples by electrodeposition in the form of thin foils and to measure their magnetoresistance characteristics and magnetic properties at room temperature. It should be noted here, however, that whereas Co foils containing hcp phase only could easily be fabricated by electrodeposition, the preparation of deposits containing fcc-Co only was not completely successful since the presence of a small fraction of the hcp phase could not be avoided under any deposition conditions explored here. Anyway, the fully hcp–Co and the predominantly fcc-Co deposits were found to have distinctly different magnetic and magnetotransport parameters.

There has been also previous knowledge about the magnetic properties of the two Co phases, especially concerning the difference in their magnetic softness in terms of saturation field and coercivity. Early studies have revealed that a single crystal of hcp-Co can be saturated along its *c*-axis in a magnetic field of a few hundred oersteds [18] whereas the saturation field in the basal plane is beyond 10 kOe [72]. For polycrystalline hcp-Co, saturation was achieved at 13 kOe [73]. On the other hand, magnetic saturation for a single crystal of fcc-Co could be achieved already at about 0.5 kOe at 550 °C in the crystallographic directions (111), (110) and (100), with the rate of approach to

saturation decreasing in the above sequence of orientations [74], a behavior completely in agreement with that of a single crystal of Ni [75]. The difference in the saturation behavior of hcp-Co and fcc-Co derives from their different magnetocrystalline anisotropies which is much larger for an hcp than for an fcc phase [75]. In line with this, it was found in the present study that the fcc-Co phase has a much lower coercive force and saturation field than hcp-Co and the field-dependence of the MR(*H*) curves corroborated these features.

As to the AMR, we have already noticed in an earlier work on electrodeposited Co [31] that the AMR ratio increased with an increasing fraction of the fcc phase in the deposits, but this effect was not considered in detail since the focus of interest was different in that previous investigation. The systematic study of the present work, however, clearly revealed that AMR(fcc-Co) ≈ 1.8 AMR(hcp-Co) which is a hitherto unknown, completely new result. Since the details of the calculated electronic density of states (DOS) around the Fermi level are different for the hcp and fcc phases of Co [65], it is actually not surprising that their AMR ratios are also found to be different from each other.

The paper is organized as follows. In Section 2, the preparation details for Co electrodeposition, the characterization methods (XRD, TEM and scanning electron microscopy (SEM)) as well as the magnetoresistance and magnetic property measurement techniques will be presented. The experimental results for structural studies are given in Section 3. Section 4 is devoted to the presentation and discussion of our magnetic data for the hcp and fcc phases of Co. In Section 5, the magnetoresistance data obtained on the electrodeposited Co foils will be described and analyzed, together with a comparison of our results with previous MR reports on Co metal and with a brief discussion in view of the recent developments on the microscopic mechanisms of the AMR. A summary of the present work will be given in Section 6.

2. Experimental

2.1. Sample preparation

For the deposition of the Co samples, a room-temperature aqueous electrolyte solution containing 100 g/L $CoSO_4$ (from $CoSO_4{\cdot}7H_2O$, Alfa Aesar) and 45 g/L H_3BO_3 (Merck) was used. Both solid compounds were of analytical grade. The *pH* of the solution was set to the required values by the addition of NaOH or H_2SO_4 for increasing or decreasing the *pH* of the solution, respectively. It is noted that the *pH* values given later in the tables are mostly those measured before deposition. It turned out that after depositing a layer of about 5 μm thickness, the bulk *pH* value was reduced by typically 0.2–0.4 and for such samples, the average of the two measured *pH* values is given in the tables (the *pH* decrease is due to the anode reaction on the Pt counter electrode).

The Co layers were electrodeposited on a Si/Cr(5 nm)/Cu(20 nm) substrate where both the Cr adhesion layer and the Cu substrate layer ensuring a conductive surface were prepared by evaporation on the Si wafer. The electrodeposition was performed in a tubular cell with an upward facing cathode completely filling the 8 mm × 20 mm recess at the bottom of the cell in order to ensure the lateral homogeneity of the deposition conditions and to avoid edge effects [76,77].

Electrodeposition was carried out with direct current at room temperature from the above bath with various *pH* values. The actual values of pH and deposition current density *j* applied will be summarized later when presenting the results of the structural studies of the deposits.

It was observed in our study that a high *pH* value of ≈5 with applied low current density ≈5 mA/cm^2 is a successful technique for producing 100% pure hcp-Co foil at room temperature. With increasing the current density to 20 mA/cm^2, a pure hcp structure was also obtained, but the deposited Co layers contained many cracks and did not adhere to the substrate; this may be due to a high strain caused by high *pH* and a higher current density. On the other hand, at a relatively low *pH* value of around 3 and an applied high current density of 150 mA/cm^2, deposits with predominantly fcc-Co were obtained. A low *pH* below 2, combined with a similarly high current density, resulted in a mixture of fcc and hcp phases in the Co deposits. Moreover, the increase of the applied current density above 150 mA/cm^2 did not yield a higher fraction of the fcc phase. A possible explanation for this can be that under these conditions the effects of pH and current density mutually interfere in that the strong H_2 evolution due to the high current density leads to a drastic local increase of the *pH* at the cathode surface, which favors the formation of the hcp Co crystals, especially if the local current density is much lower than the average one near the H_2 bubbles.

In conclusion, the lattice structure of deposited Co is sensitive to both *pH* value and applied current density, and the optimum values to get hcp-Co are *pH* of ≈5 with applied current density 5 mA/cm^2, and *pH* of ≈3 with applied current density of 150 mA/cm^2 are favorable for the preparation of the fcc-Co structure.

Several independent series of electrodeposited Co foils with a typical thickness of about 5 μm were prepared and each series consisted of 3 to 5 samples deposited under various conditions to obtain hcp-Co and fcc-Co deposits as much as possible. The nominal intended thickness was set by the electrodeposition parameters on the basis of Faraday's law by taking into account that at the low current densities used for hcp-Co preparation, the current efficiency is about 90–95 % whereas at the high current density required for the fcc-Co samples, the current efficiency is much less (typically around 35 %). Cross-sectional electron microscopy investigations were used to determine the actual deposit thicknesses. For example, in the TEM images to be shown in Section 3 which show the cross-section of the samples from the bottom to the top, the scale bars evidence the approximately 5 μm thickness for both hcp and fcc samples. The same thicknesses were obtained also from cross-sectional SEM images.

2.2. XRD studies

The phase composition of the Co deposits was investigated by XRD [78]. For most of the samples, preliminary XRD studies have been performed by CuKα radiation (wavelength: 0.15418 nm) using a Smartlab diffractometer in Bragg-Brentano configuration while the samples were still on their substrates. Based on these measurements, it turned out that due to the crystallographic texture only a few reflections can be detected using this conventional diffraction geometry. Therefore, it was decided to carry out more detailed XRD measurements with both reflection and transmission configurations on some selected samples as described below. For this purpose, XRD patterns were recorded in the range of 2θ from 40° to 130° by an X-ray diffractometer using monochromatic CoKα_1 radiation (wavelength: 0.1789 nm) and a single–crystal Ge monochromator. In these experiments, Co characteristic X-rays were applied instead of CuKα radiation since in the former case the fluorescence scattering of the Co material is much lower, thereby improving the quality of the measured XRD patterns.

Two-dimensional (2D) imaging plates were used for detecting the scattered X-rays. The intensity for each 2θ angle in the patterns was obtained by integrating the intensity along the Debye–Scherrer rings recorded on the 2D detector plates. Before the measurements, the Co films were removed from the substrate in order to avoid the appearance of substrate peaks in the diffractograms and to make the samples transparent for X-rays since diffraction experiments were performed in both reflection and transmission configurations. After the removal of the samples from the substrate, the thickness of the films was reduced from ≈5 μm to ≈1 μm electrolytically at 5 °C and 20 V by using electrolyte A3 supplied by Struers. Fig. 1a and b show schematically the reflection and transmission diffraction geometries. A very narrow parallel incident X-ray beam was used in the experiments (width: 0.2 mm, height 2 mm). The angle between the film surface and the incident beam was constant during the measurements (about 20° and 40° for reflection and transmission configurations, respectively, as shown in Fig. 1).

The patterns obtained on the two imaging plates were put together for making the full diffractograms. The complementary application of

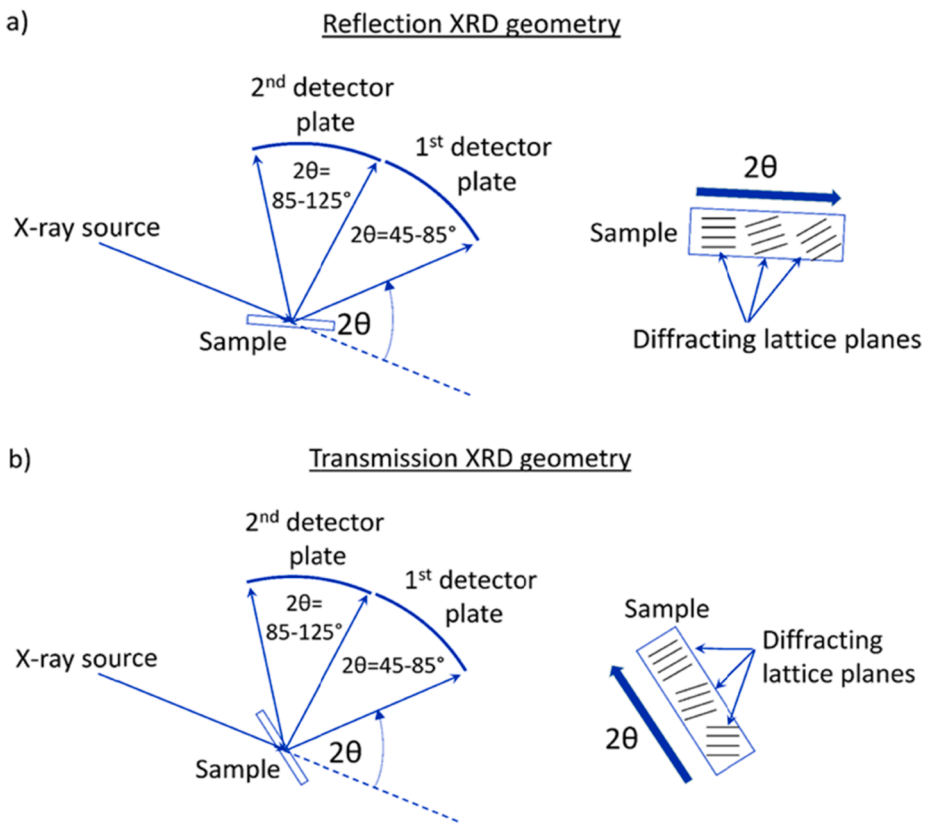

Fig. 1. Schematics showing the (a) reflection and (b) transmission geometries used in the XRD experiments. The orientation of the diffracting planes relative to the film surface is also shown at the right side of the figure. This orientation changes with increasing 2θ angle as indicated by the thick arrows.

the reflection and transmission configurations enables to obtain more reflections when the sample has a strong crystallographic texture such as usual for electrodeposited layers. Fig. 1 also shows schematically the orientation of the reflecting planes for both diffraction geometries. It should be noted that the angle between film surface and diffracting planes varies with increasing the 2θ angle of the diffraction peak as revealed in Fig. 1. Nevertheless, for reflection and transmission geometries the diffracting planes are nearly parallel and perpendicular to the film surface, respectively.

Based on the broadening of the XRD peaks, the crystallite size was determined. The physical broadening of the profiles is caused by both the size and strain effects which can be separated by the Williamson–Hall method [79]. Due to the anisotropic (i.e., *hkl* dependent) broadening of the XRD peaks caused by lattice defects such as dislocations and stacking faults, the crystallite size was estimated by analyzing the breadth of a harmonic reflection pair. Thus, for the fcc phase, the full widths at half maximum (denoted as FWHM with the unit of 1/nm) of peaks (1 1 1) and (2 2 2) were plotted as a function of the magnitude of the diffraction vector (denoted as g with the unit of 1/nm). Then, a straight line was fitted to the two points on the Williamson–Hall plot and the reciprocal of the intercept of this line with the vertical axis yielded an estimate of the crystallite size. For the hcp phase, the peak pair (0002) and (0004) were used in the Williamson–Hall plot.

It should be noted that although the more detailed XRD analysis with the CoKα_1 radiation was carried out on some selected samples only, the essential features of the obtained results are valid for all the samples processed under similar conditions (corresponding to fully hcp or predominantly fcc structures) as suggested by the XRD measurements performed with CuKα radiation.

2.3. TEM and SEM investigations

The microstructure of one fully hcp-Co and one predominantly fcc-Co sample was also investigated by TEM using a Cs corrected Themis (Thermo Fisher) TEM operated at 200 kV (spatial resolution in HRTEM mode 0.8 Å). SAED patterns were recorded by a 4kx4k Ceta camera using Velox software (Thermo Fischer). The diffraction patterns were exported in 16–bit tiff format and 1D diffraction profiles containing intensity distribution as a function of scattering angle were obtained using Process diffraction software [80]. The thinning of the FIB–cut lamellae of the samples for the TEM studies was carried out with a Thermo Scientific Scios 2 dual-beam system using 30 keV Ga^+ ions. The final steps of the thinning procedure were performed at 2 keV.

Chemical analysis was carried out by energy-dispersive X-ray spectroscopy in a TESCAN MIRA3 scanning electron microscope equipped with an EDAX Element analyzer on the same two Co foils investigated by TEM. Some little C and O signals were detected for both samples which are very probably surface impurities only (and which are always present in the SEM energy-dispersive X-ray spectra). Besides C and O, neither metallic nor other non-metallic impurities were observed up to the detection limit (about 0.1 at.% in our method for elements with atomic number>10) in both Co foil samples. Surface morphology studies have also been performed on these samples by the SEM equipment.

2.4. Measurement of the magnetoresistance characteristics and magnetic properties

For the magnetoresistance measurements, the whole Co deposit (8 mm × 20 mm) on its Si/Cr/Cu substrate was used. Since the deposits were several micrometers thick, the shunting effect of the thin Cr and Cu buffer layers could be neglected. The resistivity of the Co deposits was measured by applying a d.c. current along the longer edge of the deposit

in a four-point-in-line probe with flat gold-coated spring contacts which were sufficiently wide to ensure a homogeneous current distribution over the whole width of the Co deposits.

The MR measurements were performed at room temperature in the current-in-plane and field-in-plane configuration in magnetic fields up to $H = 8$ kOe. The MR(H) curves were measured with two orientations of the magnetic field with respect to the current: field parallel to the current flow (longitudinal MR = LMR) and field perpendicular to the current flow (transverse MR = TMR). From the saturation values of the longitudinal and transverse MR components obtained by an extrapolation of the MR(H) data from the magnetically saturated (single-domain) region to $H = 0$, the anisotropic magnetoresistance (AMR) ratio was deduced.

The MR(H) curves were measured by cycling the magnetic field from $H_{max} = +8$ kOe to $H_{max} = -8$ kOe, then back again to $H_{max} = +8$ kOe. The MR ratio at a magnetic field H was defined with the formula $MR(H) = \Delta R/R_o = [R(H) - R_o]/R_o$ where $R(H)$ is the resistance in an external magnetic field H and R_0 is the resistance maximum/minimum close to zero magnetic field.

The in-plane magnetization isotherms $M(H)$ were measured in a SQUID magnetometer at 300 K up to $H = 50$ kOe.

3. Structural studies of the electrodeposited Co foils

3.1. hcp-Co: High pH and low deposition current density

Table 1 summarizes those samples which were deposited from baths with high pH and with low deposition current density and which proved to exhibit a fully hcp structure. All these samples were investigated by XRD and on sample MET-11, a TEM study was also carried out.

3.1.1. XRD investigations

Detailed XRD results and their analysis will be presented below for sample MET-11. These data can be considered as representative since all the other samples listed in Table 1 exhibited very similar characteristics.

Fig. 2 shows the XRD patterns of sample MET-11 recorded both in reflection and transmission geometries. The intensity is plotted in logarithmic scale in order to show as many peaks as possible even if they have low intensity.

The two patterns are significantly different, indicating a considerable crystallographic texture. Nevertheless, we can clearly identify seven unique reflections [$(10\bar{1}0)$,$(10\bar{1}1)$,$(10\bar{1}2)$,$(10\bar{1}3)$,$(20\bar{2}0)$, $(20\bar{2}1)$ and (0004)] of the hcp lattice and three very close pairs of hcp and fcc reflections: hcp (0002)/fcc(111), hcp $(11\bar{2}0)$/fcc(220) and hcp $(11\bar{2}2)$/fcc(311). Since no unique reflection of the fcc lattice was observed, the coincident reflections are most probably related to the hcp phase. However, the existence of an fcc phase cannot be completely excluded since due to texture some fcc peaks may completely disappear from the pattern. The common hcp/fcc peaks cannot be used for proving or excluding the existence of the fcc phase. The TEM study described below will provide further support that this sample probably consists of the hcp phase only.

Table 1
Deposition conditions (bath pH and deposition current density j) of electrodeposited Co foils with hcp structure. The magnetoresistance parameters in the last three columns will be discussed in Section 5.

Sample code	pH	j (mA/cm^2)	H_p (Oe)	AMR ratio (%)	High-field slope, m (%/kOe)	
					LMR	TMR
MET-11	5	5	73	1.23	+0.0038	−0.0042
MET-21	5	10	–	–	–	–
MET-31	4.2	5	50	1.17	+0.0061	−0.0052
MET-32	3.9	10	–	–	–	–
MET-35	5	5	55	1.14	+0.0003	−0.0056
MET-37	4.9	10	45	1.23	−0.0025	−0.0070

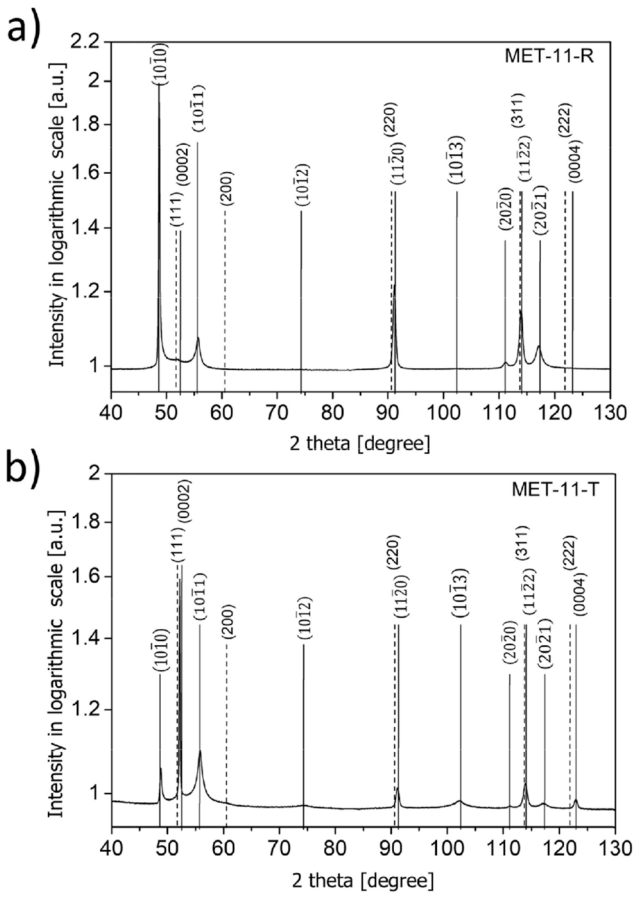

Fig. 2. XRD patterns of sample MET-11 measured in reflection (a) and transmission (b) configurations. The vertical solid and dashed lines indicate the positions of the specified Bragg reflections of the hcp-Co and fcc-Co phase, respectively.

From the peak positions of the XRD patterns recorded in the Bragg–Brentano geometry in reflection mode, the lattice parameters were determined for samples MET-11 [$a = 0.2507(2)$ nm; $c = 0.408(4)$ nm; $c/a = 1.627(4)$] and MET-21 [$a = 0.2507(2)$ nm; $c = 0.409(4)$ nm; $c/a = 1.631(4)$]. The measured lattice constants agree within the specified error with the standard reference lattice constants [66] for hcp-Co [$a = 0.2505$ nm; $c = 0.4070$ nm]. The average 1.629(4) of the two measured c/a ratios also agrees within error with the reference value ($c/a = 1.625$). These data confirm that the electrodeposited hcp-Co samples consist, indeed, of pure Co with the hcp phase.

The crystallite size of the main hcp phase was estimated by the Williamson–Hall method applied to the diffraction peak pair (0002) and (0004) as described in Section 2.2. Fig. 3 shows the Williamson–Hall plot obtained from the transmission measurement of sample MET-11. The crystallite size was estimated as the reciprocal of the intercept of the straight line fitted to the points and the vertical axis and this yields a crystallite size of about 900 ± 500 nm. It should be noted that this value is around the upper limit of detection of the crystallite size from diffraction peak breadth, therefore its uncertainty is very high.

A similar crystallite size value is obtained from the Williamson–Hall method if it is applied to the peak pair $(10\bar{1}0)$ and $(20\bar{2}0)$ of the diffractogram taken in reflection configuration since in that case reflections (0002) and (0004) are very weak due to the texture. Comparing the patterns obtained in the two diffraction geometries and considering the orientation of the diffracting planes (see Fig. 1), it seems that the hexagonal c-axis is lying parallel to the film surface in sample MET-11.

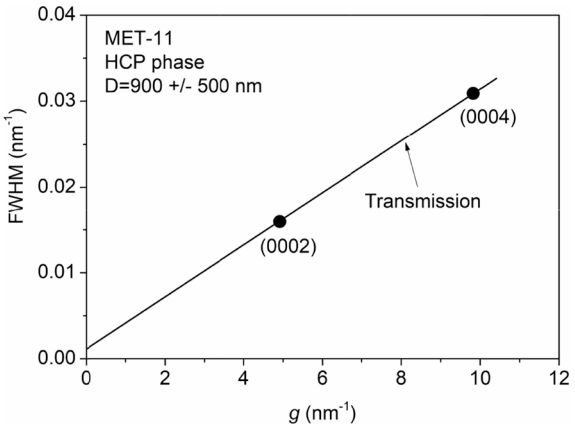

Fig. 3. Williamson–Hall plot of harmonic peak pairs (0002) and (0004) for the hcp phase in sample MET-11. The peaks were measured in transmission configuration. The crystallite size D estimated as the reciprocal of the intercept of the fitted line with the vertical axis is also shown. Ordinate axis: full width at half maximum FWHM $= \cos\theta \times \Delta(2\theta)/\lambda$ where θ is the Bragg angle, $\Delta(2\theta)$ is the breadth of the XRD peak and λ is the wavelength of X-rays; abscissa axis: magnitude of the diffraction vector $g = 2\sin\theta/\lambda$.

3.1.2. TEM studies

Two cross-sectional TEM images, a SAED pattern and the TEM diffraction intensity profile derived from the SAED pattern are displayed in Fig. 4 for sample MET-11 which was identified as hcp-Co by XRD. It can be inferred from the lower magnification image (upper left panel) that the foil thickness is about 5 μm. Both TEM images reveal a columnar growth of the Co layer as typical for atom-by-atom deposition processes and that the column widths are several hundreds of nanometers. It is also noted that the SAED pattern of sample MET-11 consists of rather well-defined diffraction spots indicating fairly large grains in agreement with the result of the XRD study.

The TEM intensity profile corresponds well to the XRD patterns of the same sample (cf. Fig. 2). The TEM study thus strongly supports the conclusion of the XRD investigation that sample MET-11 consists of hcp-Co phase and the probability of the presence of fcc-Co crystallites is very low.

3.2. fcc-Co: low pH and high deposition current density

Table 2 summarizes those samples which were deposited from baths with low *pH* and high deposition current density and which proved to exhibit a predominantly fcc structure. All these samples were investigated by XRD and on sample MET-16, a TEM study was also carried out.

3.2.1. XRD investigations

Detailed XRD results and their analysis will be presented below for sample MET-41. These data can be considered as representative since all the other samples listed in Table 2 exhibited very similar characteristics.

Fig. 5 shows the XRD patterns of sample MET-41 recorded in both the reflection and transmission geometries. The intensity distributions in the two patterns are definitely different due to the crystallographic texture. Nevertheless, both patterns contain unique peaks of fcc and hcp phases, indicating that the two structural Co modifications coexist in this sample.

The fractions of the fcc and hcp phases can be described by the contributions of the two phases to the integrated intensity of the full measured pattern. The integrated intensity is calculated as the area under the peaks after background subtraction. The intensity ratio is a good estimate of the volume ratio of the fcc and hcp phases since the two Co modifications have very similar atomic packing densities (both the fcc and hcp phases are close-packed structures). The difficulty of this evaluation is caused by the crystallographic texture and the coincident peaks. Namely, we do not know how the intensity in the coincident peaks is shared between the two phases. For overcoming this issue, the following procedure was applied.

First, the integrated intensities of the unique peaks for each phase were determined and summed up. In this step, the overlapping peaks are separated by fitting the profiles with analytical functions (e.g., Lorentzian). From the official ASTM XRD card of each phase, we determined the sum of the nominal intensity percentages of these unique peaks. The strongest peak has a nominal intensity of 100%. The numbers of the applied cards were 01-077-7453 [66] and 00-015-0806 [67] for the hcp and fcc phases, respectively. Then, the experimentally determined intensity sum of the unique peaks was divided by the sum of the nominal percentages of the same peaks. Thus, we obtained a value for each phase which gives the scattered intensity equivalent to 1% nominal intensity. Hereafter, these values are referred to as equivalent intensities for the fcc and hcp phases. Then, the integrated intensity of each coincident peak is shared between the two phases in accordance with the expected intensities. For instance, for the coincident hcp (0002)/fcc (1 1 1) peaks, the expected intensity of fcc(1 1 1) peak was calculated as the product of the equivalent intensity of the fcc phase and the nominal percentage intensity of the peak taken from the XRD card. The same was calculated for the hcp(0002) peak. Then, the measured integrated intensity of the coincident hcp (0002)/fcc(1 1 1) peak is shared between the fcc and hcp phases in accordance with the ratio of the expected intensities of the two phases. Finally, the experimentally determined integrated intensities of the two phases were summed up for all peaks (including the unique peaks and the decomposed coincident peaks) and the ratio of these two sums estimates the volume ratio of the two phases. In the final step, the volume fractions obtained from the reflection and transmission measurements were averaged for each sample. Of course, this procedure is only an approximation due to the crystallographic texture in the films. Nevertheless, for sample MET-41 the fcc and hcp fractions were 77% and 23%, respectively. For sample MET-46, similar values were obtained for the fcc and hcp fractions (73% and 27%, respectively).

From all peak positions of the XRD patterns recorded in the Bragg–Brentano geometry in reflection mode, the fcc lattice parameters were determined for samples MET-34 [$a = 0.3543(3)$ nm], MET-41 [$a = 0.3545(4)$ nm] and MET-46 [$a = 0.3545(2)$ nm]. When using the (2 0 0) and (2 2 2) reflections only, similar values were obtained: MET-34 [$a = 0.3542(4)$ nm] and MET-41 [$a = 0.3546(4)$ nm]. The average of these lattice constants is $a = 0.3544(2)$ nm which complies very well with the standard reference value [67]: $a = 0.3545$ nm. This also justifies that the majority of these "predominantly fcc-Co" samples indeed corresponds to the standard fcc-Co phase.

The Williamson–Hall plot for the (1 1 1) and (2 2 2) peak pair of the fcc phase is shown in both reflection and transmission configurations for sample MET-41 in Fig. 6. The crystallite sizes determined from the reflection and transmission measurements for this sample were about 50 nm and 100 nm, respectively. Similar results were obtained for the hcp phase in sample MET–41. It should be noted that the crystallite sizes determined from the patterns taken in reflection and transmission configurations characterize the dimensions of the crystallites mostly parallel and perpendicular to the film surface, respectively. It is also worth noting that the crystallite size for specimen MET-41 (predominantly fcc-Co with a small fraction of hcp–Co) is much smaller than that for sample MET-11 (fully hcp-Co).

This is in good agreement with the general trends established for electrodeposition that the increase in current density leads to grain refinement [81,82]. Also, the difference in the apparent crystallite sizes of the in-plane and surface normal directions may be due to the columnar growth.

3.2.2. TEM studies

Two cross-sectional TEM images, a SAED pattern and the TEM diffraction intensity profile derived from the SAED pattern are displayed

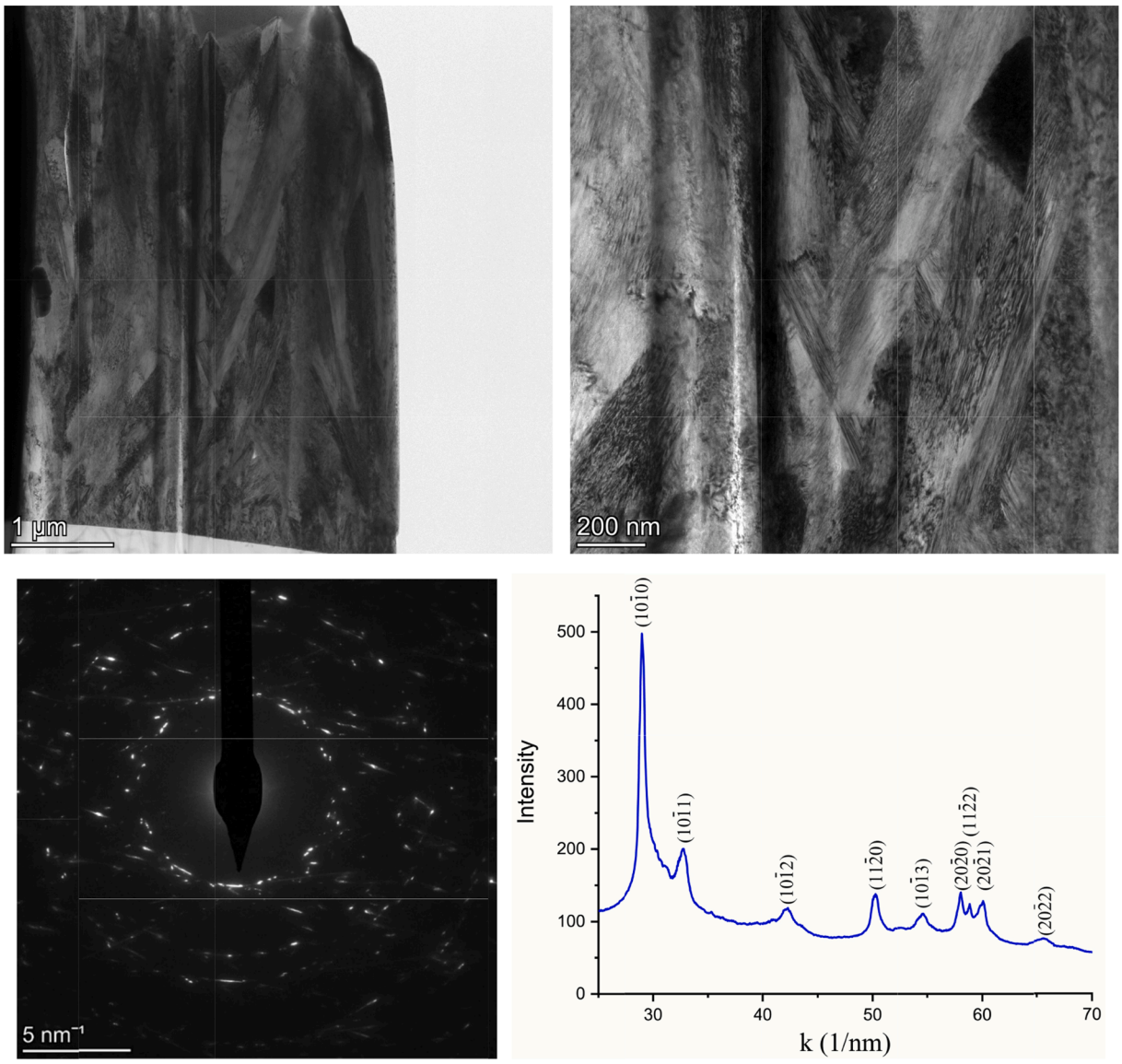

Fig. 4. Cross-sectional TEM images at two magnifications (upper panels; the growth direction is upwards), a SAED pattern (lower left panel) and the TEM diffraction intensity profile (lower right panel) derived from the SAED pattern for sample MET-11. On the abscissa axis, the wave number was obtained as $k = 4\pi \times \sin\theta/\lambda$ where θ is the Bragg angle and λ is the wavelength of electron radiation. The identified Bragg reflections of the hcp-Co lattice are specified above the corresponding diffraction peaks.

Table 2
Deposition conditions (bath *pH* and deposition current density *j*) of electrodeposited Co foils with predominantly fcc structure. The magnetoresistance parameters in the last three columns will be discussed in Section 5.

Sample code	*pH*	*j* (mA/cm^2)	H_p (Oe)	AMR ratio (%)	high-field slope, *m* (%/kOe)	
					LMR	TMR
MET-16	2	150	10	1.91	−0.0075	−0.0093
MET-33	2.2	150	15	1.73	−0.0059	−0.0073
MET-34	2	200	16	2.19	−0.0052	−0.0084
MET-41	2.6	150	17	1.93	−0.0085	−0.0160
MET-46	3.4	150	20	2.00	−0.0059	−0.0101
MET-47	4.2	150	18	1.83	−0.0080	−0.0086

in Fig. 7 for sample MET-16 which was identified by XRD as containing predominantly fcc-Co crystallites with some hcp-Co phase fraction as well. The lower magnification image (upper left panel) reveals that the foil thickness is about 5 μm. As for sample MET-11 (hcp-Co, Fig. 4), both TEM images reveal also here a columnar growth with much narrower column widths. This is in agreement with the result of the XRD study (see Fig. 6) of another predominantly fcc-Co sample (MET-41) which has a much smaller crystallite size than sample MET-11 (hcp-Co). It is also noted that the diffraction spots of the SAED pattern of sample MET-16 are less well-defined than those of sample MET-11, also indicating smaller grains for the predominantly fcc-Co sample in comparison with the fully hcp-Co sample.

As to the TEM intensity profile of sample MET-16, it contains two relatively intense unique hcp peaks [hcp (10$\bar{1}$0) and hcp (10$\bar{1}$1)] as well as several unique hcp peaks up to (20$\bar{2}$2) with very low intensity. We can also clearly see a unique fcc(200) peak. There are furthermore three strong coincident peak pairs: hcp (0002)/fcc(111), hcp (11$\bar{2}$0)/fcc (220) and hcp (11$\bar{2}$2)/fcc(311) which can belong to any one of the hcp or fcc phases. The visible fcc(200) peak definitely indicates the presence of fcc crystallites in the sample.

The angular resolution of the SAED pattern does not allow establishing if the coinciding hcp (0002)/fcc(111) and hcp (0004)/fcc(222) peaks

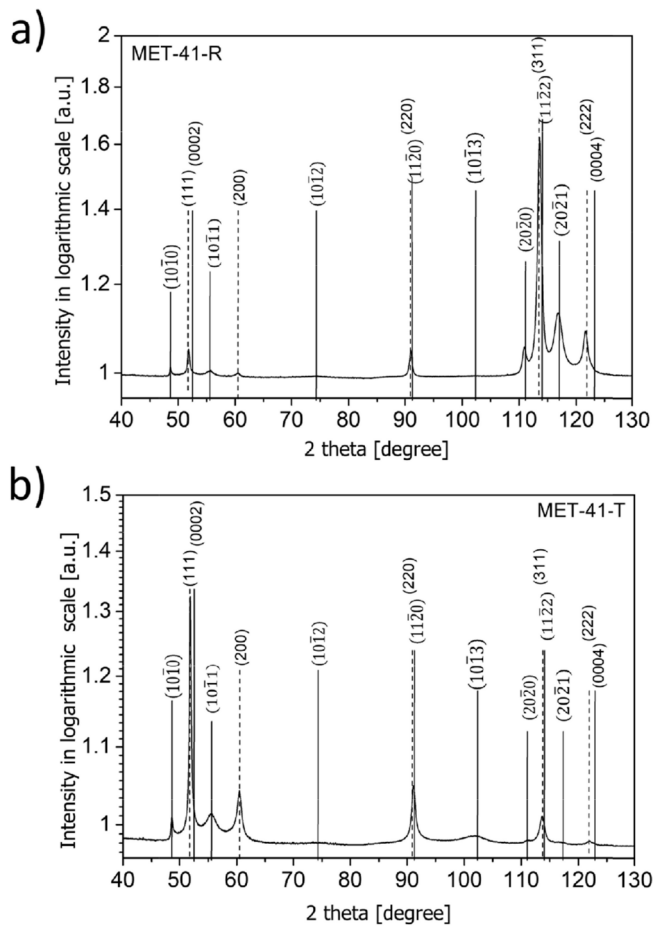

Fig. 5. XRD patterns of sample MET-41 measured in reflection (a) and transmission (b) configurations. The vertical solid and dashed lines indicate the positions of the specified Bragg reflections of the hcp-Co and fcc-Co phase, respectively.

belong to the fcc-Co phase or to the hcp-Co phase. However, we have also recorded the XRD pattern for this sample which, due to its sufficient resolution, revealed that these peaks actually belong to the fcc phase (cf. also the XRD patterns of sample MET-41 in Fig. 5). Due to the high intensity of the fcc(111) peak, this implies that there should be a substantial fraction of fcc crystallites in sample MET-16.

On the other hand, it is also clear that the presence of hcp crystallites is not negligible. Consequently, the TEM SAED observations are in agreement with the phase constitution assessment derived from the XRD data, i.e., the specimen is predominantly fcc-Co containing some hcp-Co phase fraction as well.

3.3. Electrodeposited Co samples with comparable fractions of hcp-Co and fcc-Co phases

During the deposition experiments in an effort to explore the deposition conditions promoting either hcp or fcc phase formation, several samples were prepared which proved to contain a comparable amount of both hcp-Co and fcc-Co phases according to their XRD patterns. The deposition parameters of these samples are listed in Table 3, together with the magnetoresistance parameters of a few of the mixed-phase samples.

3.4. Surface morphology of the electrodeposited Co samples of various phases

The crystalline form of the grains in the electrodeposited samples significantly impact the surface morphology of the deposits as demonstrated in Fig. 8. Samples with hcp structure (e.g., sample MET- 11) are composed of lamellae with mean plane nearly perpendicular to the substrate plane. These deposits are slightly porous. In contrast, Co samples with (predominantly) fcc structure (e.g., MET-33) exhibit pyramid-like coalescent grains with no cavities in between. The surface morphologies found are conformal to those of electrodeposited Co-Ni alloys of the corresponding crystal structure [83,84]. Interestingly, the typical surface morphology of electrodeposited fcc-Ni with some specific texture is also similar to our fcc-Co deposits [85]. A smoother deposit surface and a smaller apparent grain size were obtained for mixed-phase Co deposits (see SEM image of sample MET-4). This is in accord with the general observation that a grain size minimum can be achieved in the deposition regime where two crystalline phases coexist [30]. Under such circumstances, the frequent nucleation of both crystal types leads to limited-range growth and the coexisting grains of various phases mutually hinder the growth of each other.

Whereas it is a general observation that the actual grain size in the

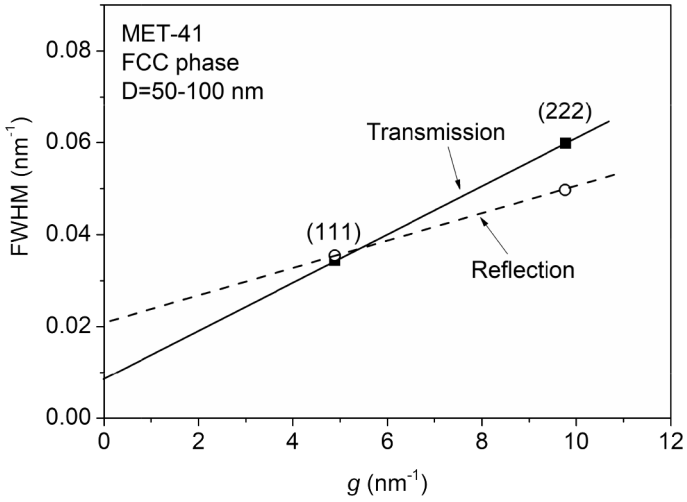

Fig. 6. Williamson–Hall plot of harmonic peak pairs (111) and (222) for the fcc phase in sample MET-41. The peaks were measured in both reflection and transmission configurations. The crystallite size D estimated as the reciprocal of the intercept of the fitted line with the vertical axis is also shown. Ordinate axis: full width at half maximum FWHM $= \cos\theta \times \Delta(2\theta)/\lambda$ where θ is the Bragg angle, $\Delta(2\theta)$ is the breadth of the XRD peak and λ is the wavelength of X-rays; abscissa axis: magnitude of the diffraction vector $g = 2\sin\theta/\lambda$.

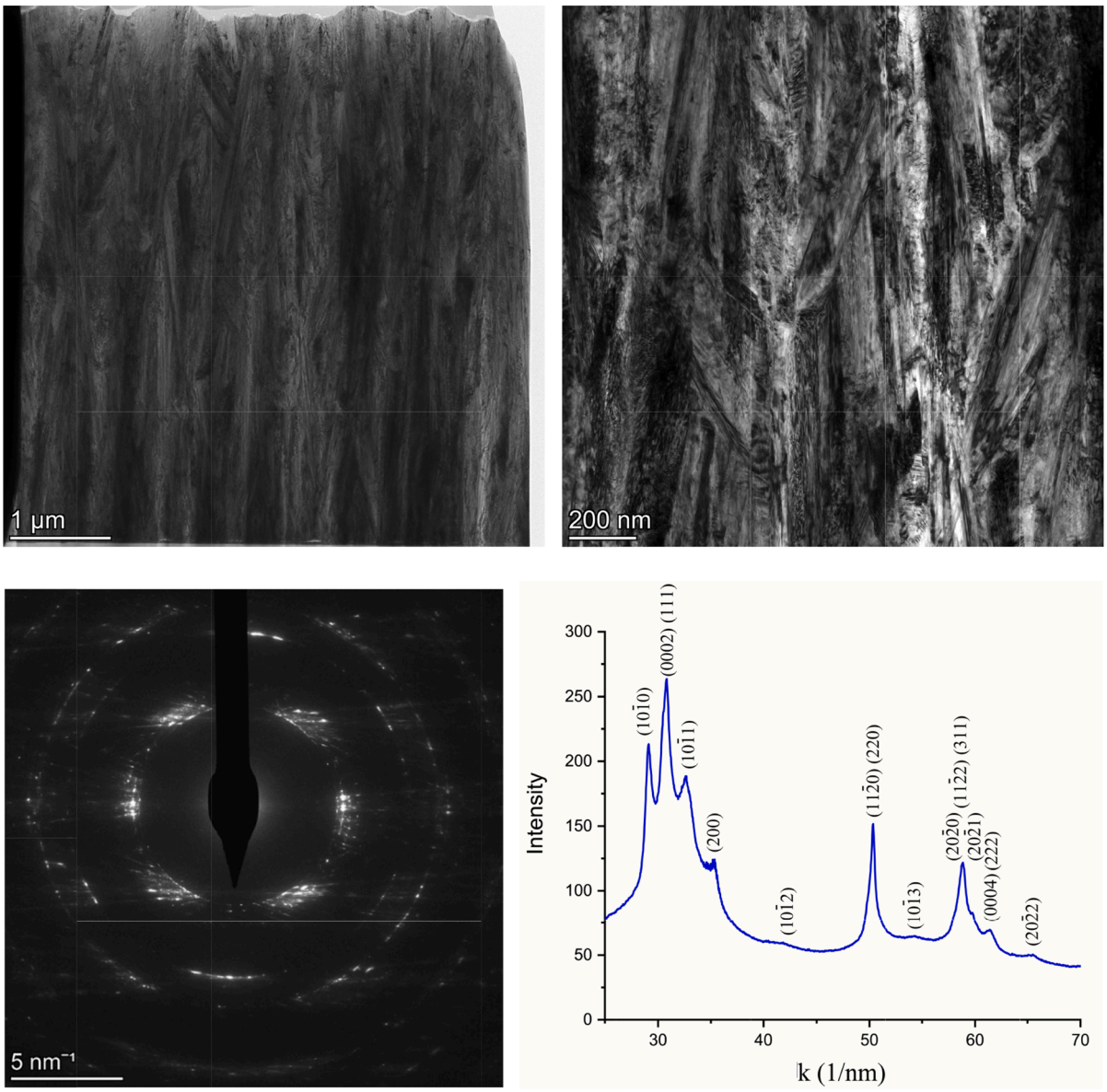

Fig. 7. Cross-sectional TEM images at two magnifications (upper panels; the growth direction is upwards), a SAED pattern (lower left panel) and the TEM diffraction intensity profile (lower right panel) derived from the SAED pattern for sample MET-16. On the abscissa axis, the wave number was obtained as $k = 4\pi \times \sin\theta/\lambda$ where θ is the Bragg angle and λ is the wavelength of electron radiation. The identified Bragg reflections of the hcp-Co and fcc-Co lattices are specified above the corresponding diffraction peaks.

Table 3
Deposition conditions (bath *pH* and deposition current density *j*) of electrodeposited Co foils which were found by XRD to contain comparable fractions of the hcp and fcc phases. The magnetoresistance parameters in the last three columns will be discussed in Section 5.

Sample code	*pH*	*j* (mA/cm^2)	H_p (Oe)	AMR ratio (%)	high-field slope, *m* (%/kOe)	
					LMR	TMR
MET-1	2.6	5	–	–	–	–
MET-2	2.7	10	–	–	–	–
MET-3	2.5	30	16	1.44	−0.0056	−0.0077
MET-4	2.7	50	–	–	–	–
MET-5	2.6	90	5	1.49	−0.0096	−0.0100
MET-13	2.5	90	–	–	–	–
MET-15	2.7	81	–	–	–	–
MET-23	1.6	125	–	–	–	–
MET-24	1.5	150	–	–	–	–
MET-43	2.0	150	25	1.39	−0.0117	−0.0151

interior of layers obtained via atom-by-atom deposition processes is smaller (sometimes much smaller) than the surface features visible, it is also found that the smaller the surface granule size the smaller the grain size is [86,87]. This trend is clearly visible also in Fig. 8 since the crystallite size as deduced from the XRD studies presented above was found to be by an order of magnitude smaller for predominantly fcc samples (like MET-33) than for the fully hcp sample MET-11, the latter exhibiting a much rougher surface than the former.

4. Magnetic properties

The magnetic properties were investigated for two electrodeposited Co samples: MET-11 (fully hcp, see Table 1) and MET-16 (predominantly fcc, see Table 2). For both samples, the magnetization isotherm *M* (*H*) was measured by a SQUID magnetometer at room temperature up to $H = 50$ kOe magnetic field. The *M*(*H*) data agreed very well in the two cases when the magnetic field was oriented along the same direction as the current during the measurement of the longitudinal MR and when H

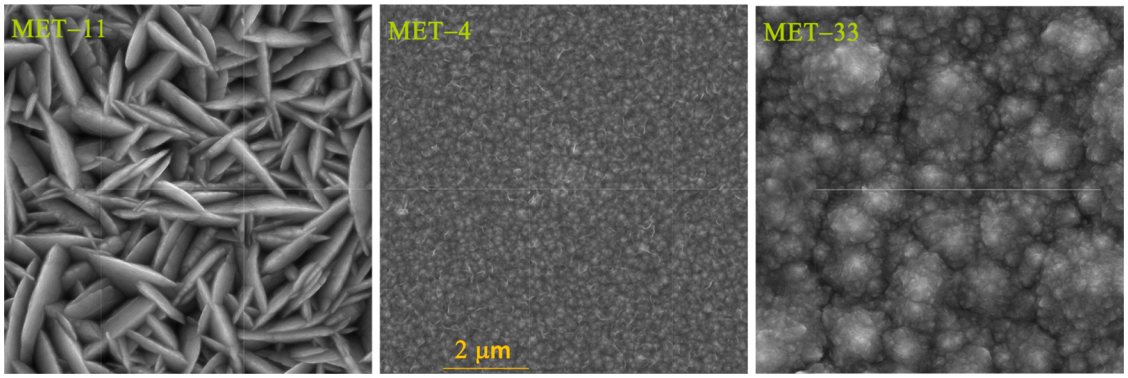

Fig. 8. SEM image of the surface of three electrodeposited Co samples having hcp (MET–11), mixed hcp + fcc (MET-4) and predominantly fcc (MET-33) phases.

was perpendicular to the current direction corresponding to the measurement of the transverse MR.

Since the magnetization showed a very small increase above about 10 kOe for both the hcp and fcc phases, for better visibility, the normalized magnetization data M/M(50kOe) are shown in Fig. 9 for lower fields only. One can observe in Fig. 9 that whereas for our polycrystalline fcc–Co sample the magnetization reaches almost full saturation at around 2 kOe, the magnetization of our polycrystalline hcp-Co sample approaches saturation around 8 kOe only. This can be traced back to the high magnetocrystalline anisotropy of hcp-Co as opposed to the magnetically much more isotropic character of fcc–Co that was already discussed in detail in the Introduction on the basis of Refs. [72–75].

For a better illustration of understanding the different magnetic behavior of the two crystalline phases of Co metal, in Fig. 9 we have also displayed the $M(H)$ curves reported for a bulk polycrystalline hcp-Co sample [73] as well as for bulk single-crystal hcp-Co samples, for the latter with the magnetic field oriented either along the c–axis which corresponds to the magnetic easy axis or in the basal plane in which any direction corresponds to a magnetic hard axis. For the easy-axis orientation of single-crystal hcp-Co, we have displayed in Fig. 9 the result from Ref. 73 which data indicate a saturation around 3 kOe whereas for the single-crystal hcp-Co reported in Ref. 72 (data also reproduced in Ref. 75), saturation was achieved already in about 2 kOe. Furthermore,

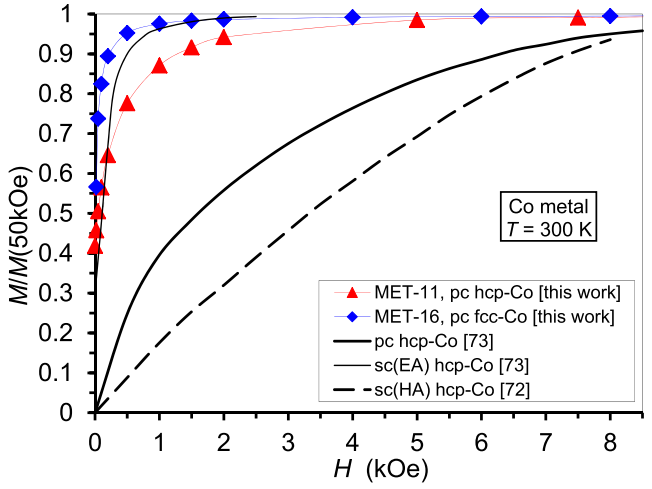

Fig. 9. Room-temperature magnetization isotherms $M(H)$ for the hcp-Co sample MET-11 and the predominantly fcc-Co sample MET-16. For comparison, the $M(H)$ curves reported for polycrystalline (pc) and single-crystal (sc) hcp-Co are also displayed. For sc hcp-Co, EA and HA denote measurements with the magnetic field along the magnetic easy axis (hcp c-axis) and along a hard axis (in the hcp basal plane), respectively.

Masumoto et al. [18] reported saturation in a magnetic field of about 0.3 kOe for a rod-shaped hcp-Co single crystal with the c-axis along the rod length. Apparently, the actual easy-axis saturation field strongly varies for the different single-crystal hcp-Co samples investigated, reflecting probably differences in sample quality and purity. The slow saturation in the basal plane (see Fig. 9) taken from Ref. 72 was reproduced even quantitatively also by Masumoto et al. [18] up to their maximum magnetic field of 1 kOe. The polycrystalline hcp-Co $M(H)$ data in Fig. 9 were taken from Ref. 73 and the data in Ref. 18 measured up to 1 kOe show a similar behavior although by some 20 % larger values for a given magnetic field.

One can see in Fig. 9 that our polycrystalline fcc-Co sample approaches to saturation at very low fields comparable to those reported for single-crystal hcp-Co samples along the easy axis. The large magnetocrystalline anisotropy of hcp–Co is illustrated by a comparison of the $M(H)$ curves of a single crystal of hcp-Co along the easy axis and along a hard axis in the basal plane, in the latter direction the magnetization reaching saturation in magnetic fields beyond 10 kOe only [72].

Fig. 9 reveals, furthermore, that the $M(H)$ curves of polycrystalline hcp-Co samples go between the $M(H)$ curves of a single crystal of hcp-Co measured along the c-axis and in the basal plane. This is expected since the magnetization of polycrystalline hcp-Co corresponds to some average of the $M(H)$ curves of a single crystal of hcp-Co in the magnetic easy and hard directions. Since any direction in the basal plane of the hcp crystal corresponds to a hard axis, for a random (texture-free) bulk polycrystal of Co the $M(H)$ curve is expected to lie closer to the $M(H)$ curve measured in the basal plane than to that measured along the c-axis as we can indeed observe in Fig. 9. On the other hand, the $M(H)$ curve of our polycrystalline hcp-Co sample (MET-11) lies much closer to the $M(H)$ curve of the single crystal of hcp-Co measured along the c-axis. The reason for this is that according to the XRD study (see Section 3.1.1), this hcp-Co sample has a strong texture in that the hexagonal c-axis (i.e., the easy axis) of most of the crystallites lies in the deposit plane in which the magnetic field is applied. Therefore, our textured hcp-Co polycrystal foil can be more easily magnetized with an in-plane magnetic field than a random bulk hcp-Co polycrystal studied in Ref. 73.

One can conclude in general that the behavior of the approach to saturation in our two investigated samples is well in compliance with the results of structural studies claiming that sample MET-11 consists of a pure hcp-Co phase whereas sample MET-16 consists mainly of a fcc-Co phase.

The different magnetic behaviors deduced from the approach to saturation of the $M(H)$ curves for our hcp-Co and fcc-Co samples above are fully corroborated by the coercive field data which can be obtained from Fig. 10. Here, the $M(H)$ curves were measured when coming with the magnetic field from saturation at $H = 50$ kOe to negative field values. The data reveal that whereas the coercive field H_c is about 75 Oe for the hcp-Co sample, H_c can be estimated to be <10 Oe for the fcc-Co sample. These coercive field values properly reflect the large difference

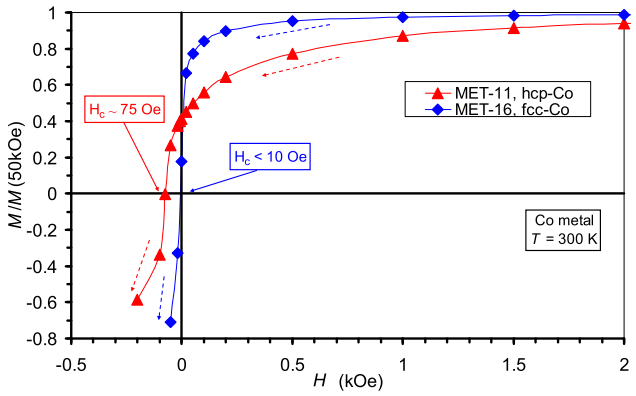

Fig. 10. Low-field magnetization data for the hcp-Co and fcc-Co samples to determine the coercive field H_c of the two Co phases. The dashed-line arrows indicate the direction of the variation of the magnetization when recording the $M(H)$ data.

in the magnetocrystalline anisotropy of the two Co phases.

The results on our samples agree well with previous reports on the coercive force of electrodeposited Co. Cerisier et al. [88] found $H_c = 8$ Oe for their fcc-Co deposits and an increase of the coercive force to 23 Oe for Co deposits with some hcp-Co fraction. Armyanov and Vitkova [89,90] performed a particularly detailed study of the dependence of H_c on the hcp-Co fraction in their Co deposits. They found that H_c is about 20 Oe for a hcp-Co volume fraction of about 35 % and H_c reaches values around 80 Oe for fully hcp-Co deposits, the latter finding being in good agreement with our result. Although at $T = 100$ K Bhuiyan et al. [91] obtained much larger coercivity values (fcc-Co: 50 Oe, hcp-Co: 270 Oe) than our values, these data also show that H_c of the hcp-Co phase is much larger than that of the fcc-Co phase.

In our previous work on electrodeposited Co/Cu multilayers [92], it was found that for Cu spacer layers below about 1 nm where the Cu layer is not continuous and, thus, the Co layers are interconnected through pinholes in the spacer, the coercive field values are smaller than 20 Oe. Since the multilayer stack as a whole exhibited an fcc structure [93], these data also show comparable coercive fields to our present bulk fcc-

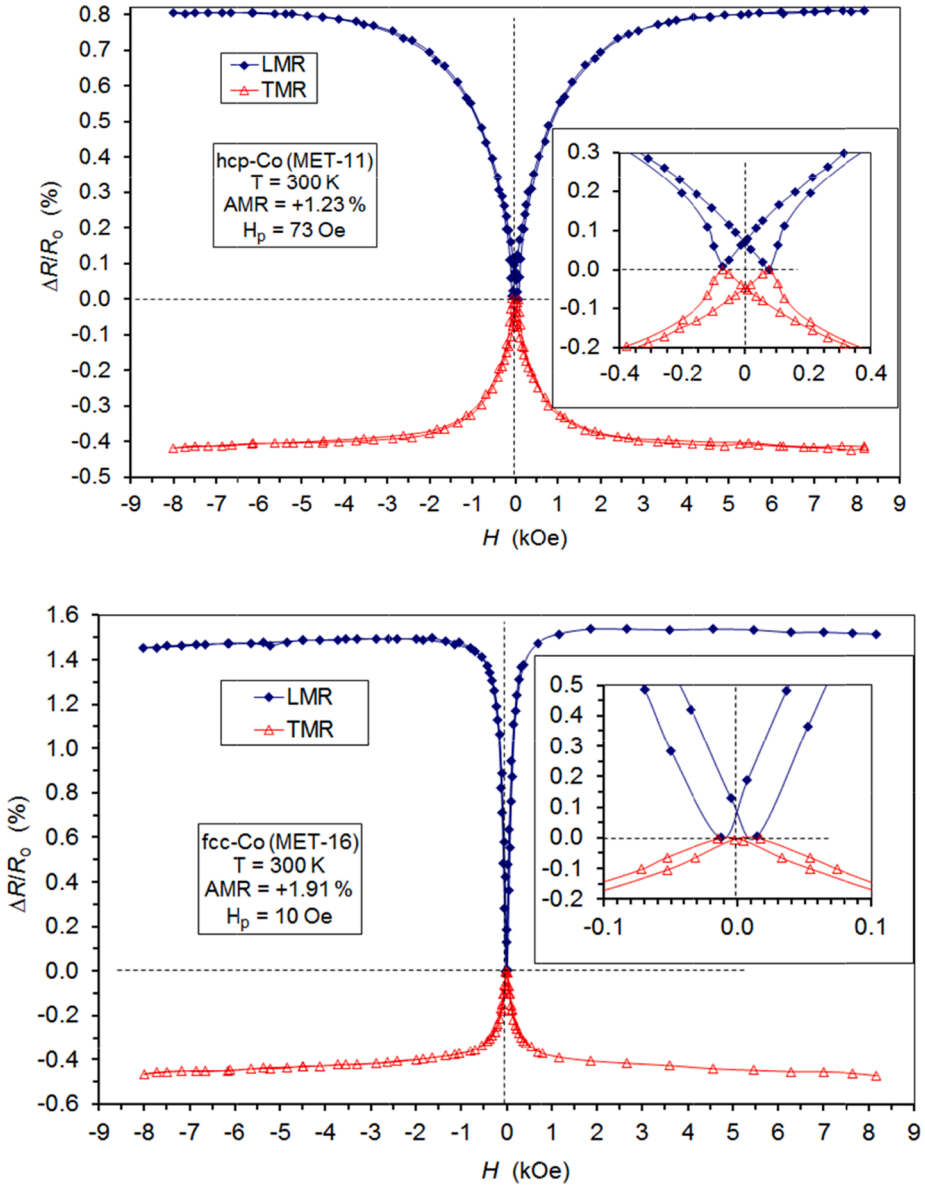

Fig. 11. Longitudinal (LMR) and transverse (TMR) magnetoresistance curves for hcp-Co (upper panel) and fcc-Co (lower panel). The insets show the MR(H) curves for low magnetic fields in order to reveal the hysteresis behavior.

Co deposit. Low coercive fields (below about 40 Oe) have been observed also on electrodeposited Co thin films with thicknesses 20 to 200 nm [38,94,95], in which thickness range finite-size effects do not play a role in the coercivity. Although no structural studies were reported for these films, in view of the present results we can conclude that these Co thin films certainly have contained a significant fraction of fcc phase as well.

5. Magnetoresistance studies

5.1. Magnetoresistance results on the present electrodeposited Co samples

The room-temperature magnetoresistance was measured for several of the present electrodeposited Co foils and their measured magnetoresistance parameters are given in Tables 1–3. Here, we will present first in detail the results for those two samples only for which the magnetic properties were reported in Section 4: sample MET-11 (hcp) and sample MET-16 (predominantly fcc). Afterwards, a general discussion of these parameters for the investigated Co samples will follow.

The LMR(H) and TMR(H) curves for the two selected samples are shown in Fig. 11. One can observe the same difference in the approach to saturation for the MR(H) curves of the two different Co phases as could be seen also in the corresponding M(H) curves (Fig. 9). Whereas the MR (H) curves reach saturation already around 2 kOe for the predominantly fcc-Co sample which is indicated by the practically linear behavior afterwards, the saturation begins to be complete around 8 kOe only or even above for the hcp-Co sample.

We compare here briefly the LMR(H) curve of our hcp-Co foil with the longitudinal magnetoresistance results of Masumoto et al. [18] on rod-shaped hcp-Co single crystals and polycrystals. In agreement with the magnetization, the MR(H) curves also saturated in a magnetic field of about 0.3 kOe when the c-axis (easy axis) of the hcp-Co single crystal was oriented along the rod length. Correspondingly, for single crystals with the rod axis lying in the basal plane, i.e., in the hard direction, the MR(H) curves showed a very slow increase with magnetic field with no sign of saturation up to 1 kOe. On the other hand, for a polycrystal rod of hcp-Co, the resistance increase with magnetic field was 0.33 % at their maximum field of 1 kOe and this compares well to our LMR(H) data for the polycrystalline hcp-Co foil (see upper panel in Fig. 11).

The insets in Fig. 11 display the low-field data on an enlarged scale to reveal a hysteresis of the MR(H) data and to determine the MR(H) peak positions H_p which agreed well for the LMR and TMR components for both samples. Their values were found to be H_p(hcp-Co) = 73 Oe and H_p(fcc-Co) = 10 Oe. These results match fairly well the coercive field values obtained for the same hcp-Co (H_c = 75 Oe) and fcc-Co (H_c < 10 Oe) samples in Section 4, reflecting also properly the magnetically much softer behavior of the dominating fcc-Co phase in the latter sample.

The determination of the AMR ratio was made according to the procedure of Refs. 48 and 49. First, the results for the clearer case of fcc-Co will be discussed. It can be observed (Fig. 11, lower panel) that the MR(H) curves for both the LMR and TMR components show a decreasing behavior with increasing magnetic field in the magnetically saturated region (above about 2 kOe). This resistivity change with the field is due to the gradual suppression of magnons by increasing the field which diminishes the resistivity contribution due to electron scattering on magnons [22,46,49,51]. This MR contribution is approximately linear in the field range of our investigation and, therefore, a linear fit was applied to the data above magnetic saturation. The intercept of the linear fits with the ordinate axis yielded the zero-field saturation values of the longitudinal and transverse magnetoresistance components for the fcc-Co sample: $LMR_s = +1.52$ % and $TMR_s = -0.39$ %. Since the AMR ratio defined in the Introduction as AMR = $\Delta\rho_{AMR}/\rho_{is}$ can be rewritten also as AMR = $(\rho_{Ls} - \rho_{Ts})/\rho_{is} = LMR_s - TMR_s$ by assuming that ρ_{is} is equal to the zero-field resistivity which is usually a good approximation [22,49,52], we get finally AMR = +1.91 % for sample MET-16 which consists of mainly fcc-Co with some fraction of the hcp-Co phase as well.

For the hcp-Co phase (sample MET-11), we cannot proceed in a similarly straightforward manner due to the much lower rate of approach to saturation as a consequence of the high magnetocrystalline anisotropy of this phase. Nevertheless, the TMR component seems to become approximately linear for sufficiently high fields and we can apply a linear fit with good fit quality for the data above about 3 kOe from which we get $TMR_s = -0.38$ %. As to the LMR(H) data for hcp-Co, we can proceed as follows. One can see that the slope is positive even if we consider only the data points at the highest fields, i.e., we have not yet reached saturation at our highest magnetic field of 8 kOe. Therefore, we extrapolate from the LMR(8kOe) = +0.82 % value to zero field by assuming the same slope for the LMR component beyond our maximum field as obtained for the TMR component. This procedure ends up with an estimated value of $LMR_s = +0.85$ %. From these data, we get finally AMR(hcp-Co) = (1.23 ± 0.10) % for sample MET-11 where the specified error was obtained by considering the uncertainty due to the non-saturated state up to 8 kOe.

The other hcp-Co (Table 1) and predominantly fcc-Co (Table 2) samples investigated exhibited similar MR(H) curves corresponding to the behavior of samples MET-11 and MET-16, respectively. The MR(H) curves of samples with comparable fractions of the hcp and fcc phases (Table 3) resembled mainly the behavior of the predominantly fcc-Co samples. The values of the MR(H) peak position H_p, the AMR ratio and the high-field slope m were derived for all measured samples in a similar manner as described above and are summarized in Tables 1–3. Below we will first analyze the AMR ratio and H_p data and later come back to the discussion of the high-field slope data.

One can see from Tables 1 and 2 that the average value of the AMR ratios for hcp-Co is 1.19 % and for the samples with predominantly fcc-Co phase is about 1.92 %. By assuming a volume additivity of the AMR ratios for a predominantly fcc-Co sample with a typical fraction (25 %) of the hcp-Co phase (see the estimate of the hcp-Co fraction in Section 3.2.1 for two such samples), we end up with an assessed AMR ratio of about 2.16 % for the pure fcc-Co phase.

It should be noted that the AMR ratios of the hcp-Co samples show a relatively small scatter whereas the scatter of the data for the predominantly fcc-Co samples is much larger. The reason for this is that the samples listed in Table 1 all exhibit fully hcp structure whereas the samples listed in Table 2, although exhibit predominantly an fcc structure, but still contain some fraction of the hcp-Co phase as well. The fraction of the hcp-Co phase may change from sample to sample and, thus, the relative contribution of the hcp and fcc phases to the AMR ratio will also be different.

It is interesting to note that the mixed-phase samples listed in Table 3 which contained comparable amounts of hcp-Co and fcc-Co crystallites had AMR ratios between 1.4 and 1.5 %. These intermediate AMR values correspond well to the mixed-phase state of these samples.

It is now worth recalling our previous work on the AMR of mixed hcp-Co and fcc-Co phases [31] mentioned already in the Introduction in which AMR ratios from 1.5 to 2.2 % were reported for estimated fcc-Co fractions from 15 to 50 %. Although a similar XRD technique was used for structural characterization, a much less accurate approach was applied there for estimating the hcp/fcc fractions than in the present work and this may explain that the decomposition with our new data for the pure hcp and fcc phases does not properly match the actually measured values of the earlier work [31]. Another source of discrepancy can be that in the earlier work the samples were prepared under quite different conditions (e.g., using very different baths) than in the present study and, therefore, the microstructural features of the two sets of samples may be markedly different. Nevertheless, even the old AMR ratios fit well into the general trend of the present data.

In order to better assess the present magnetoresistance results summarized in Tables 1–3, we display these data in Fig. 12 in the form of a correlation between the AMR ratio and the MR(H) peak position H_p. The AMR ratio for the hcp-Co samples is around 1.2 % and their H_p values are the largest among all the samples due to the high magnetocrystalline anisotropy of hcp-Co; nevertheless, the H_p values scatter in a range due

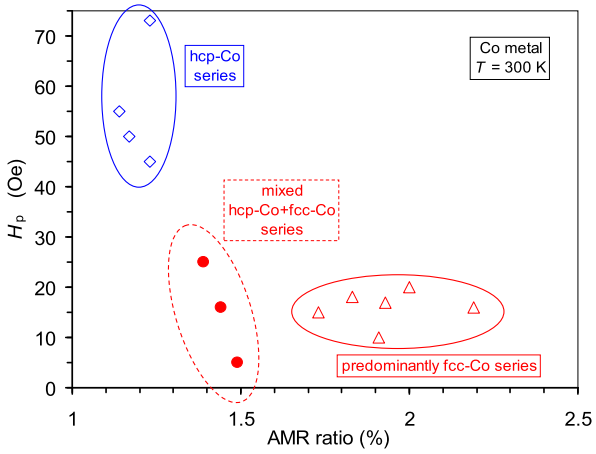

Fig. 12. Correlation between the MR(H) peak position H_p and the AMR ratio for the electrodeposited Co samples with various phase constituents.

to the possible differences of the microstructural features and texture between the individual samples. The predominantly fcc-Co samples have the highest AMR ratios whereas their H_p values are fairly small due to the small magnetocrystalline anisotropy of the dominating fcc-Co phase. The data for the mixed-phase samples with comparable fractions of the hcp-Co and fcc-Co phases are situated, as expected, in between both concerning the AMR ratio and the peak field value.

It was already noted above that for the hcp-Co samples the LMR(H) curves usually did not reach saturation in the highest magnetic field of 8 kOe applied here and this is the reason that for the hcp-Co samples the slope of the m(LMR) curve had a very small negative value or it had even a positive value (see Table 1). In lack of a sufficiently high magnetic field to reach saturation, we needed to apply a special procedure for getting an estimate of the LMR_s values. Although this procedure implies a small uncertainty of the AMR values for the hcp-Co samples as specified above, there is some systematic correlation between the high-field slope values of the LMR and TMR components which will be considered now.

Fig. 13 displays a diagram of the m(LMR) vs. m(TMR) data for all the investigated Co deposits by using the results in the three tables. The positive m(LMR) values for some hcp-Co samples indicate that for these samples saturation was definitely not reached up to $H = 8$ kOe. As noted beforehand, the predominantly fcc samples and the mixed-phase samples exhibited rather similar behavior and reached saturation in similarly low magnetic fields; correspondingly, their data points are well

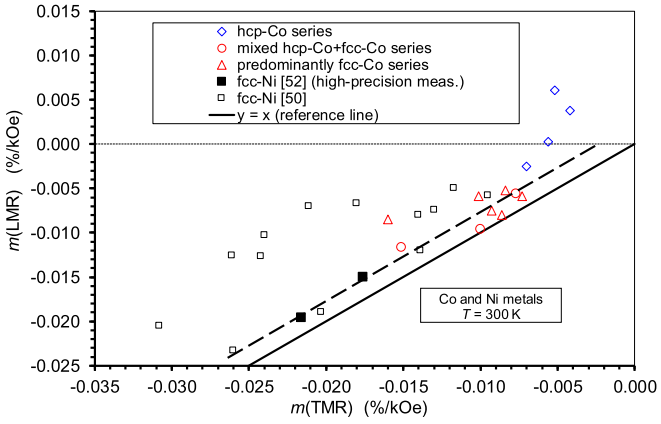

Fig. 13. Correlation between the slope m of the LMR and TMR components of the MR(H) curves for electrodeposited Co samples with various phase constituents and for fcc–Ni from previous studies as indicated in the legend. The thick dashed line corresponds to the intrinsic difference of the two slopes with respect to the reference line (see text for more details).

intermixed with each other in Fig. 13. The thick solid line corresponds to the m(LMR) = m(TMR) relation. The experimental data are all above this reference line, indicating that for each sample with negative m(LMR), the magnitude (absolute value) of m is smaller for LMR than for TMR. We can also observe that the appearance of the data points in this diagram is not random, but they rather seem to be distributed in a zone approximately parallel to the reference line.

In order to demonstrate that this is a general phenomenon, we have added further data to this diagram which were obtained on various bulk and nanocrystalline Ni samples in the same magnetoresistance setup as used in the present work. These samples were investigated in our previous work [50] where the AMR ratios and the m values averaged over the LMR and TMR components were reported. By using the original m (LMR) and m(TMR) results, in Fig. 13 we included now these data by the open squares which evidently follow the same general trend as the data for the present Co samples. One should notice, however, that the Ni data are shifted in the diagram generally to higher m values for both components with respect to the Co samples. This difference is quite reasonable by considering the more than twice as large Curie temperature of Co in comparison with Ni [75]. Namely, due to its much lower Curie temperature, in Ni metal there is much stronger thermal disorder of the magnetization at room temperature and, therefore, the application of an external magnetic field in the magnetically saturated state can induce a much stronger alignment of the disordered magnetic moments which then results in a larger resistivity decrease in a given magnetic field in comparison with Co metal.

Now we will turn to a discussion of explaining why the data points in the diagram of Fig. 13 lie above the reference line for which there may be two reasons.

First, the resistivity change in the magnetically saturated state is negative for both the LMR and the TMR components due to the gradual suppression of the thermally induced spin disorder as explained above. However, this negative change in resistivity is slightly counteracted for the LMR component by the fact that with increasing the magnetic field the resistivity increases in the LMR configuration until reaching the magnetically completely saturated state. Even if it looks in a measurement that the M(H) curve is apparently already in saturation, a very small degree of further domain alignment will yield an increasing resistivity counteracting the similarly small negative resistivity change due to the paraprocess, i.e., the more and more perfect alignment of individual magnetic moments by the external magnetic field against the thermally induced disorder. On the other hand, it is easy to see that the two processes have the same sign, i.e., both of them contribute a negative resistivity change for the TMR component. This difference between the LMR and TMR slopes does not appear only if the magnetic field is sufficiently high and we can have data definitely beyond the true technical magnetic saturation. Apparently, for most of the Ni and Co samples displayed in Fig. 13 this was not the case since a magnetic field of $H = 8$ kOe may not have been always sufficient to reach complete magnetic saturation as evidenced by all the data being placed above the reference line.

However, we have recently carried out a high-precision magnetoresistance study of a bulk and a nanocrystalline Ni sample at room temperature up to several tens of kilooersted [52]. This study has unambiguously revealed that the resistivity decrease in the magnetically completely saturated state is indeed stronger for the TMR component than for the LMR component. An evident explanation for this difference can be that the transverse spin fluctuations are more effectively suppressed by the external magnetic field than the longitudinal spin fluctuations which explanation, however, still needs a theoretical justification. Nevertheless, the firm experimental findings of Ref. 52 are included in Fig. 13 by the two solid squares. Both data points are slightly above the reference line by roughly the same distance and we have added a thick dashed line through them which runs parallel with the reference line. Since these data were obtained in high-precision measurements in the magnetically completely saturated state, we can

consider that they represent the intrinsic deviation, at least for Ni metal, from the reference line in sufficiently high magnetic fields where "intrinsic" refers to the fact that the deviation is only due to the difference in the magnon suppression process between the LMR and TMR configurations. Any deviation from the reference line by more than the thick dashed line running through the two high-precision data points parallel to the reference line indicates that the result was derived from measurements in not sufficiently high magnetic fields; any measurement inaccuracy is, of course, superimposed on top of all this (e.g., the data points lying almost on the reference line certainly have a large error).

5.2. *Evaluation of previous data on the magnetoresistance of Co metal in view of the present results*

In the following, we will briefly review earlier results on the magnetoresistance behavior of Co metal. The first report on the magnetoresistance of Co can be traced back to Tomlinson [3,4] in the early 1880s who established that LMR > 0 by measuring the resistivity of metallurgically prepared Co rods in a magnetic field. In 1887, Faé [5] and Goldhammer [6] demonstrated by measurements on electrodeposited Co foils that, similarly to Ni and Fe [1,2], Co metal also exhibits the AMR phenomenon, i.e., LMR > 0 and TMR < 0.

The first quantitative study of the magnetoresistance of Co metal was reported by Goldhammer [7] in 1889 by investigating Co foils electrodeposited on platinized glass, without giving any specific details of the deposition conditions. The tabulated magnetic field vs. resistivity data of Ref. 7 for four electrodeposited Co foils are displayed in Fig. 14 which reveals astonishing similarities to our data in Fig. 11. First, sample Co-4 in Fig. 14 approaches saturation apparently at much higher fields only than the other samples and it has the lowest AMR ratio (1.05 %). In view of our result on our hcp-Co sample MET-11, it is appealing to assign a predominantly hcp structure to sample Co-4 of Ref. 7. The highest AMR ratio (1.93 %) of sample Co-5 with a low saturation field strongly resembles the behavior of our predominantly fcc-Co sample in Fig. 11. The other two samples of Ref. 7 have intermediate AMR ratios and low saturation fields, just as obtained on our above discussed mixed-phase samples with comparable fractions of the hcp and fcc phases. Evidently, Goldhammer [7] could not yet be aware of the two crystalline phases of Co that time (in 1889), well before the discovery of X-rays and

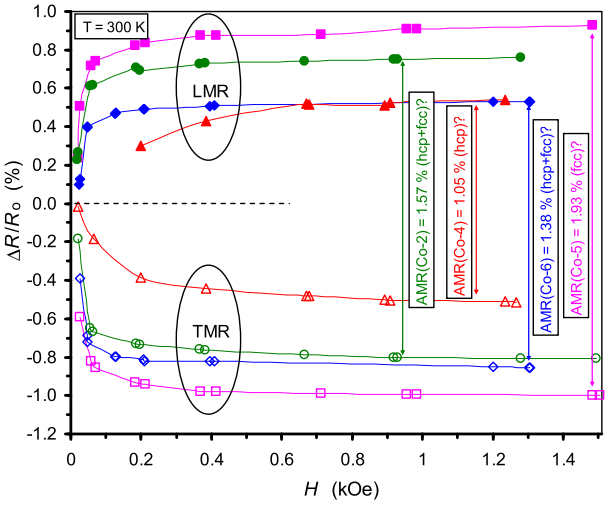

Fig. 14. Longitudinal (LMR) and transverse (TMR) magnetoresistance curves for the four electrodeposited Co foils investigated by Goldhammer [7]. We have assigned the difference of the LMR and TMR values taken at the highest magnetic field to the AMR ratios of each sample as indicated with the vertical double-headed arrows. The notation about structure with question mark is our guess on the basis of the MR data and structural analysis of the samples of the present paper.

their diffraction on crystals, but a comparison with our results clearly reveals the possible phases of his samples. Goldhammer [7] tried to ascribe the observed differences to the different magnetic prehistory of the samples (e.g., whether the LMR or the TMR component was measured first) and he observed some systematic differences, but these effects are fairly small and they are eliminated in our measurements when measuring full field cycles starting always from saturation.

There were numerous subsequent magnetoresistance studies of Co metal, but in many cases either the LMR or the TMR component was only measured with typical (absolute) values between 0.5 % and 1 % [8–10,12,13,16,18,21]. By considering that mostly no crystal structure data were provided, these values correspond well to the range of data obtained for our various samples.

We will discuss briefly the reported AMR results for bulk Co samples. Bates [14] reported the room-temperature LMR(*H*) and TMR(*H*) curves for hard-drawn Co wire for which no structural characterization was given. The LMR(*H*) curve indicated saturation around 2 kOe and it became linear for higher fields reaching up to about 17 kOe. The low saturation field may speak for an fcc structure of the wire. The TMR(*H*) curve became also linear for high fields with the same slope as the LMR (*H*) curve, the slope being about m = –0.0100 %/kOe which is quite comparable to some of our values in Table 2. The difference of the LMR and TMR values at the highest fields yields an AMR ratio of 0.45 %. In view of our results, this value is definitely too small and the most probable reason for this may be the insufficient purity of the Co metal (98.4 %) used in Ref. 14, especially the presence of about 1 at.% C specified impurity may have caused a strong deleterious effect on the magnetotransport properties.

In the work of Dey [17], fairly pure Co wires with ppm level impurities only were investigated. The LMR(*H*) curves reached saturation around 10 kOe with a slight decrease for higher fields and the TMR(*H*) data indicated a slight variation of resistivity only. From the high-field data, an AMR ratio of about 1.7 % can be deduced. This value is close to our value for the predominantly fcc–Co samples whereas the high saturation field is rather characteristic of the hcp-Co phase. Unfortunately, in the lack of any structural information in the work of Dey [17], one cannot further assess the reported magnetoresistance data.

Myung and Nobe [30] investigated electrodeposited Co layers which were qualified by XRD as having an hcp structure with a crystallite size of 120 nm. Large AMR ratios (ca. 3 % and 3.5 %) were measured for two Co samples. Unfortunately, no MR(*H*) curves were reported in the paper and we cannot straightforwardly interpret their data because they evidently contradict to our present results. Their values for the AMR ratio of hcp-Co is apparently too high in view of our result AMR(hcp-Co) ≈ 1.2 %. The reported high AMR values are especially curious in view of the fact that the maximum magnetic field applied in Ref. 30 was 1.5 kOe only, since this was definitely not sufficient to saturate the magnetoresistance for the hcp-Co samples.

Due to the large interest in utilizing the AMR effect in various applications of ferromagnetic thin films [96], there have been several studies also on the magnetoresistance of evaporated and sputtered Co thin films since the early 1970s [20–26,28,33]. The reported AMR ratios range from about 0.3 % to 2.5 % and in most cases, no structural characterization and MR(*H*) curves have been presented, so it is again hard to make any further assessment about the results except the possible influence of finite film thickness effects. Namely, in very thin films, the contribution of surface scattering to resistivity cannot be neglected [97]. Therefore, since the surface scattering contribution can be taken as independent of the magnetic field, when calculating the AMR ratio $\Delta\rho_{AMR}/\rho_{is} \approx \Delta\rho_{AMR}/\rho_o$, the zero-field resistivity ρ_o is larger than the bulk value due to the surface scattering in the thin film whereas the $\Delta\rho_{AMR}$ term does not gain a contribution form the surface scattering effect. As a result, the AMR ratio will be smaller than the bulk vale. In order to illustrate this point, it is noted that an AMR ratio of about 2 % was only reported for those films where the film thickness was 100 nm or more [23–25], whereas for thinner films (20 to 55 nm) AMR ratios in the

range 0.3 % to 1 % were only obtained [20,26,33].

In the last few decades, several magnetoresistance studies were reported for individual Co nanowires, Co nanowire arrays and networks which were prepared by electrodeposition into nanoporous membranes [27,29,32,37] and for Co nanowires formed by lithographic processes [34]. The nanowire diameters were typically 100 nm, but in most cases, the crystallographic structure was not established. The reported AMR values were around 1 % which values are mostly lower limits only since the applied magnetic field was often not sufficient to saturate the resistivity in the TMR configuration due to the large saturation magnetization of Co and the high demagnetizing factor perpendicular to the nanowire direction. Nevertheless, the reported AMR values for Co nanowires are in compliance with our results on hcp-Co and fcc-Co. For thinner nanowires, one should also to take into account that similar surface scatterings effects as discussed for the very thin films may also reduce the measured AMR ratio with respect to the bulk value.

We should also mention the interesting result of Bennett and Wright [19] who measured the magnetoresistance of amorphous Co at $T = 4.2$ K and obtained AMR = 0.9 %. The amorphous state of Co was achieved by evaporation in ultra-high vacuum onto liquid–helium–cooled substrate. The amorphous state remained stable up to about 40 K where an amorphous → crystalline transformation occurred, evidenced by a sudden drop of the resistivity by a factor 4 and by the appearance of mainly hcp crystallites and a small fraction of fcc crystallites. Due to the large structural disorder, the density of states around the Fermi level in amorphous Co is definitely different from that of hcp-Co and fcc-Co and, therefore, the AMR ratio of the amorphous state may also be different. Nevertheless, the reported AMR ratio is still fairly close to the crystalline values.

It is noted finally that although no theoretical calculation of the AMR ratio of pure Co in either crystallographic phase has yet been reported, there have been calculations for fcc Co-Ni alloys [98,99]. The results of the two theoretical works are in good agreement with each other, but it was pointed out in Ref. 48 that these calculated results are larger by a factor 2 than the experimental data. The same holds true if the fcc Co-Ni alloy data are extrapolated to pure Co, the extrapolation yielding an AMR ratio larger by at least a factor 2 than our experimental data. One reason for the deficiency of theoretical calculations to reproduce the experimental AMR values is that the theoretically calculated residual resistivities still highly underestimate the experimental values [48]. More recent progress in the calculation of the finite-temperature resistivity of pure metals [100,101] will certainly enable better theoretical results also for the magnetotransport properties in the future.

5.3. On the microscopic mechanisms of the AMR in the present hcp-Co and fcc-Co samples

According to some recent papers [39,53,61,62] discussing the microscopic mechanisms of the AMR effect, the AMR contains two kinds of contribution which can be classified [39] as extrinsic ones deriving from scattering-dependent transport mechanisms and intrinsic ones deriving from scattering-independent transport mechanisms. In the canonical approach, the AMR is ascribed to extrinsic effects occurring due to scattering events (e.g., on phonons, lattice defects or impurities). The first indications of intrinsic contributions to the AMR were reported on the basis of novel experimental results and theoretical considerations [53,61]. The intrinsic contributions are usually ascribed to band structure effects which may arise, e.g., when the electronic band structure depends on the magnetization orientation [53].

From the viewpoint of the present results on the AMR of hcp-Co and fcc-Co, the results of Nádvornik et al. [39] are particularly interesting since these authors reported on the AMR of a 10-nm-thick nanocrystalline hcp-Co film with 3 to 5 nm grain sizes by using broadband terahertz measurements. They have established that hcp-Co exhibits a significant intrinsic contribution which amounts to about 2/3 of the total room-temperature AMR of about 1 %, the latter value measured by using d.c. current. The presence of an intrinsic AMR term in hcp-Co was ascribed entirely to the strongly anisotropic character of the hcp lattice. In good accordance with this conclusion, these authors [39] found from the broadband terahertz measurements that the AMR of a 10-nm-thick fcc-Ni film with similar estimated grain sizes is of predominantly extrinsic nature.

We shall make here some notes on our results in view of the above described decomposition approach to AMR. As it turned out from our structural study in Section 3, the grain size of the hcp-Co foils investigated in this work is of the order of 1 μm and, thus, these samples can be considered as corresponding to bulk hcp-Co. Since the room-temperature electron mean free path of hcp-Co is around 10 nm [102], the contribution of lattice defects to the electronic transport can be neglected in these hcp-Co samples and the dominant contribution is due to the phonon scattering. Therefore, there is definitely an extrinsic contribution to the AMR in our hcp-Co samples. However, from our findings, we cannot estimate the importance of the intrinsic contribution to the total AMR. Nevertheless, our average AMR ratio of about 1.2 % for bulk polycrystalline hcp-Co samples is in fairly good agreement with the result of Nádvornik et al. [39].

In contrast to the hcp-Co samples, according to the results of structural studies in Section 3.2, the Co-foil samples with a predominantly fcc-Co phase exhibit a nanocrystalline microstructure. It is well known [103] that the presence of a large amount of grain boundaries in the nanocrystalline regime can give a significant contribution to the resistivity. Therefore, the overall resistivity of a nanocrystalline sample will be larger than the bulk value. It has been demonstrated recently [104] that for fcc-Ni, which has a zero-field resistivity $\rho_o = 7.24$ μΩcm [105] in the bulk state at room temperature, the additional grain-boundary contribution to the resistivity is about 3 μΩcm if the grain size is around 50 nm. Since the zero-field resistivity at room temperature for polycrystalline bulk hcp-Co ($\rho_o = 6.0$ μΩcm [106]) and fcc-Co ($\rho_o = 5.5$ μΩcm [107]) is fairly close to the corresponding fcc-Ni value, we may assume that the grain-boundary resistivity contribution for both Co phases in the presently investigated predominantly fcc–Co samples will also be similar to that of Ni. All this means that in our predominantly fcc-Co samples, the extrinsic AMR, in addition to the contribution deriving from scattering on phonons, will also contain a non-negligible contribution due to scattering on lattice defects (mainly grain boundaries here).

Furthermore, as mentioned above, one of the conclusions of Nádvornik et al. [39] was that at room temperature the intrinsic AMR contribution is negligible in fcc-Ni. It is worth to mention here that in a recent work [50], we have investigated the AMR of electrodeposited Ni foils and it turned out that for crystallite sizes down to about 30 nm, the AMR ratio remains unchanged with respect to the value of the coarse-grained (bulk) state. At the smallest grain sizes investigated, the grain-boundary contribution to the zero-field resistivity is about 5 μΩcm which is quite comparable to the bulk value $\rho_o = 7.24$ μΩcm [105]). Since the AMR ratio did not vary with grain size [50], all this implies that for fcc-Ni the resistivity anisotropy splitting $\Delta\rho_{AMR}$ increased by about 70 % from the bulk state to the nanocrystalline state with the smallest grain size (30 nm). Such a substantial range of ρ_o and $\Delta\rho_{AMR}$ over which the AMR ratio remained constant was only possible if the intrinsic AMR contribution in fcc-Ni is negligible. This conclusion is in good agreement with the finding of Nádvornik et al. [39]. All these results seem to suggest, at the same time, that the intrinsic AMR contribution is probably not significant either in fcc-Co.

6. Summary

The major goal of the present work was to determine experimentally the AMR ratio for the two crystalline states of Co (hcp and fcc) since these data have not been available beforehand. For this purpose, electrodeposited Co foils were prepared under different deposition conditions based on the information accumulated in the literature [71] about

the promoting factors for hcp and fcc phase formation.

By using XRD and TEM SAED techniques for structural studies, we have succeeded in electrodepositing from a sulfate bath fully hcp-Co foils at high *pH* (ca. 5) and low deposition current density (ca. 5 mA/cm^2) whereas predominantly fcc-Co foils (with about 25 % fraction of the hcp-Co phase) were obtained for low *pH* (ca. 2 to 3) and high current density (ca. 150 mA/cm^2).

The field dependence of both the magnetization and the magnetoresistance demonstrated the expected much softer magnetic behavior of fcc-Co in comparison with hcp-Co, the latter phase exhibiting a much larger magnetocrystalline anisotropy than fcc-Co. Furthermore, it turned out from the magnetoresistance measurements that the AMR ratio is $\Delta\rho_{AMR}/\rho_{is} = 1.19$ % for hcp-Co whereas 1.92 % for the predominantly fcc-Co samples from which an AMR ratio of 2.16 % was assessed for the pure fcc-Co phase. Thus, it could be established, for the first time, that the AMR ratio is different for the two phases of Co, specifically, it is by almost a factor of 2 larger for the fcc-Co phase than for the hcp-Co phase.

As to the microscopic mechanisms of the AMR effect in Co metal, recent work by Nádvornik et al. [39] demonstrated that in hcp-Co the observed AMR is dominated by the intrinsic mechanisms. We cannot conclude anything to this issue from our data for hcp-Co, but at least our experimental AMR ratio is fairly close to that of these authors. On the other hand, based on our former AMR data for bulk and nc fcc-Ni [50], we could argue that the observed AMR of fcc-Ni does not seem to include a significant contribution from intrinsic mechanisms, in agreement again with the conclusion of Nádvornik et al. [39] for this metal. These results allow us to suggest that the AMR of fcc-Co is probably also dominated by the extrinsic mechanisms. Further work is in progress to get experimental evidence for this conjecture.

Nevertheless, since theoretical work [65] revealed different density of states for the two Co phases, the importance of band-structure effects (i.e., intrinsic mechanisms) in the AMR can also be quite different for these phases.

Author declaration

Herewith we declare that the work described has neither been published not is under consideration for publication elsewhere and that its publication is approved by all authors.

Declaration of Competing Interest

The authors declare that they have no known competing financial interests or personal relationships that could have appeared to influence the work reported in this paper.

Acknowledgements

The Wigner Research Centre for Physics utilizes the research infrastructure of the Hungarian Academy of Sciences and is operated by the Eötvös Loránd Research Network (ELKH) Secretariat (Hungary). M. El-Tahawy is indebted to the Egyptian Government for providing a post-doc fellowship to the Eötvös Loránd University, Budapest, Hungary. This research was also supported by grants no. VEKOP-2.3.3-15-2016-00002 and VEKOP-2.3.2-16-2016-00011 of the European Structural and Investment Funds. The authors are very thankful to one of the reviewers for bringing to our attention some papers about the microscopic mechanisms of the AMR effect. During the manuscript revision, the authors profited much from useful consultations with K. Palotás and L. Szunyogh.

References

[1] W. Thomson, Phil. Trans. Roy. Soc. London 146 (1856) 649.
[2] W. Thomson, Proc. Roy. Soc. London 8 (1856–1857) 546.
[3] H. Tomlinson, Proc. Roy. Soc. London 33 (1882) 276.
[4] H. Tomlinson, Phil. Trans. Roy. Soc. London 174 (1883) 1.
[5] G. Faé, Phil. Mag. Series 5, 23 (145), 540 (1887).
[6] D. Goldhammer, Ann. Physik 267 (1887) 360.
[7] D. Goldhammer, Ann. Physik 272 (1889) 804.
[8] J.C. Beattie, Philos. Mag. 45 (274) (1898) 243.
[9] L. Grunmach, Ann. Physik 327 (1907) 141.
[10] P. McCorkle, Phys. Rev. 22 (1923) 271.
[11] Y. Matuyama, Sci. Rep. Tohoku Imp. Univ., First Series 23 (1934) 537.
[12] M.S. Alam, Z. Phys. 93 (1935) 556.
[13] Y. Shirakawa, Sci. Rep. Tohoku Imp. Univ. (Honda Anniv. Vol.) (1936) 362; Sci. Rep. Tohoku Imp. Univ. 27 (1939) 532.
[14] L.F. Bates, Proc. Phys. Soc. London 58 (1946) 153.
[15] R. de Mandrot, Helv. Phys. Acta 26 (1953) 563.
[16] E.E. Semenenko, A.I. Sudovtsov, Soviet Physics JETP 20 (1965) 323.
[17] S.K. Dey, Ph.D. Thesis, Imperial College, London, U.K., 1966.
[18] H. Masumoto. H. Saito, M. Kikuchi, Sci. Rep. RITU, Ser. A 18 (1966) 84.
[19] M.R. Bennett, J.G. Wright, Phys. Lett. A 38 (1972) 419.
[20] K. Asama, K. Takahashi, M. Hirano, AIP Conf. Proc. 18 (Pt. 1) (1974) 110.
[21] P.S. Galepov, Soviet Phys. J. 17 (1974) 1243.
[22] T.R. McGuire, R.I. Potter, IEEE Trans. Magn. 11 (1975) 1018.
[23] T.R. McGuire, J.A. Aboaf, E. Klokholm, IEEE Trans. Magn. 20 (1984) 972.
[24] P.P. Freitas, A.A. Gomes, T.R. McGuire, T.S. Plaskett, J. Magn. Magn. Mater. 83 (1990) 113.
[25] S.S.P. Parkin, in: B. Heinrich, J.A.C. Bland (Eds.), Ultrathin Magnetic Structures, Vol. II, Springer-Verlag, Berlin, 1994, p. 148.
[26] M. Viret, D. Vignoles, D. Cole, J.M.D. Coey, W. Allen, D.S. Daniel, J.F. Gregg, Phys. Rev. B 53 (1996) 8464.
[27] R. Ferré, K. Ounadjela, J.M. George, L. Piraux, S. Dubois, Phys. Rev. B 56 (1997) 14066.
[28] U. Rüdiger, J. Yu, L. Thomas, S.S.P. Parkin, A.D. Kent, Phys. Rev. B 59 (1999) 11914.
[29] J.E. Wegrowe, D. Kelly, A. Franck, S.E. Gilbert, J.P. Ansermet, Phys. Rev. Lett. 82 (1999) 3681.
[30] N.V. Myung, K. Nobe, J. Electrochem. Soc. 148 (2001) C136.
[31] I. Bakonyi, E. Tóth-Kádár, J. Tóth, L.F. Kiss, L. Pogány, Á. Cziráki, C. Ulhaq-Bouillet, V. Pierron-Bohnes, A. Dinia, B. Arnold, K. Wetzig, Europhys. Lett. 58 (2002) 408.
[32] T. Ohgai, L. Gravier, X. Hoffer, M. Lindeberg, K. Hjort, R. Spohr, J.P. Ansermet, J. Phys. D: Appl. Phys. 36 (2003) 3109.
[33] W. Gil, D. Görlitz, M. Horsiberger, J. Kötzler, Phy. Rev. B 72 (2005), 134401.
[34] B. Leven, G. Dumpich, Phy. Rev. B 71 (2005), 064411.
[35] T.Y. Chung, S.Y. Hsu, J. Phys.: Conf. Series 150 (2009), 042063.
[36] X. Xiao, J.H. Liang, B.L. Chen, J.X. Li, D.H. Ma, Z. Ding, Y.Z. Wu, J. Appl. Phys. 119 (2015), 043908.
[37] T.C.S.C. Gomes, J.D. Medina, M. Lemaitre, L. Piraux, Nanoscale Res. Lett. 11 (2016) 466.
[38] S. Zsurzsa, L. Péter, L.F. Kiss, I. Bakonyi, J. Magn. Magn. Mater. 421 (2017) 194.
[39] L. Nádvorník, M. Borchert, L. Brandt, R. Schlitz, K.A. de Mare, K. Výborný, I. Mertig, G. Jakob, M. Kläui, S.T.B. Goennenwein, M. Wolf, G. Woltersdorf, T. Kampfrath, Phys. Rev. X 11 (2021) 021030.
[40] W.A. Reed, E. Fawcett, in: Proc. Int. Conf. Magnetism, Nottingham, England, 1964, p. 120.
[41] D.L. Marker, J.W. Reichardt, R.V. Coleman, J. Appl. Phys. 42 (1971) 1338.
[42] F. Battalan, I. Rosenman, Solid State Commun. 12 (1973) 75.
[43] R.V. Coleman, R.C. Morris, d.J. Sellmyer, Phys. Rev. B 8 (1973) 317.
[44] Y. Kubo, N. Shohata, H. Fujii, H. Fujiwara, T. Okamoto, J. Phys. Soc. Japan 38 (1975) 87.
[45] R.M. Bozorth, Ferromagnetism, Van Nostrand, New York, 1951.
[46] I.A. Campbell, A. Fert, Transport properties of ferromagnets, in: Ferromagnetic Materials, vol. 3, Ch. 9 ed. E.P. Wohlfarth, North-Holland, Amsterdam, 1982.
[47] R.C. O'Handley, Modern Magnetic Materials. Principles and Applications, Wiley-Interscience, New York, 2000.
[48] B.G. Tóth, L. Péter, Á. Révész, J. Pádár, I. Bakonyi, Eur. Phys. J. B 75 (2010) 167.
[49] I. Bakonyi, Eur. Phys. J. Plus 133 (2018) 521.
[50] V.A. Isnaini, T. Kolonits, Z. Czigány, J. Gubicza, S. Zsurzsa, L.K. Varga, E. Tóth-Kádár, L. Pogány, L. Péter, I. Bakonyi, Eur. Phys. J. Plus 135 (2020) 39.
[51] B. Raquet, M. Viret, E. Sondergard, O. Cespedes, R. Mamy, Phys. Rev. B 66 (2002), 024433.
[52] I. Bakonyi, F.D. Czeschka, L.F. Kiss, V.A. Isnaini, A. Krupp, K. Palotás, S. Zsurzsa, L. Péter, manuscript available from: <http://arxiv.org/abs/2203.11568>.
[53] K.M. Seemann, F. Freimuth, H. Zhang, S. Blügel, Y. Mokrousov, D.E. Bürgler, C. M. Schneider, Phys. Rev. Lett. 107 (2011), 086603.
[54] I. Turek, J. Kudrnovsky, V. Drchal, Phys. Rev. B 86 (2012), 014405.
[55] J. Kimling, J. Gooth, K. Nielsch, Phys. Rev. B 87 (2013), 094409.
[56] S. Wimmer, D. Ködderitzsch, H. Ebert, Phys. Rev. B 89 (2014), 161101.
[57] J. Chen, Y. Sakuraba, K. Masuda, Y. Miura, S. Li, S. Kasai, T. Furubayash1, K. Hono, Appl. Phys. Lett. 110 (2017) 242401, doi: 10.1063/1.4985237.
[58] C. Lidig, J. Cramer, L. Weißhoff, T.R. Thomas, T. Kessler, M. Kläui, M. Jourdan, Phys. Rev. Appl. 11 (2019), 044039.
[59] Y. Li, F. Zeng, S.S.L. Zhang, H. Shin, H. Saglam, V. Karakas, O. Ozatay, J. E. Pearson, O.G. Heinonen, Y. Wu, A. Hoffmann, W. Zhang, Phys. Rev. Lett. 122 (2019), 117203.
[60] O. Šipr, S. Wimmer, S. Mankovsky, H. Ebert, Phys. Rev. B 101 (2020), 085109.
[61] F.L. Zeng, Z.Y. Ren, Y. Li, J.Y. Zeng, M.W. Jia, J. Miao, A. Hoffmann, W. Zhang, Y. Z. Wu, Z. Yuan, Phys. Rev. Lett. 125 (2020), 097201.

[62] J.H. Park, H.W. Ko, J.M. Kim, J.M. Park, S.Y. Park, Y.H. Jo, B.G. Park, S.K. Kim, K. J. Lee, K.J. Kim, Sci. Rep. 11 (2021) 20884.
[63] T.B. Massalski (Ed.), Binary Alloy Phase Diagrams, second ed., Plus Updates on CD–ROM, ASM International, Materials Park, Ohio, USA, 1996.
[64] I. Bakonyi, Acta Mater. 53 (2005) 2509.
[65] R. Lizárraga, Fan Pan, L. Bergqvist, E. Holmström, Zs. Gercsi, L. Vitos, Sci. Rep. 7 (2017) 3778.
[66] ASTM Powder Diffraction File PDF-01-077-7453.
[67] ASTM Powder Diffraction File PDF-00-015-0806.
[68] T. Kolonits, P. Jenei, L. Péter, I. Bakonyi, Z. Czigány, J. Gubicza, Surf. Coat. Techn. 349 (2018) 611.
[69] P. Nagy, N. Rohbeck, G. Roussely, P. Sortais, J. Gubicza, J. Michler, L. Pethő, Surf. Coat. Technol. 386 (2020), 125465.
[70] A.W. Hull, Phys. Rev. 17 (1921) 571.
[71] A. Vicenzo, P.L. Cavallotti, Electrochim. Acta 49 (2004) 4079.
[72] S. Kaya, Sci. Rep. Tohoku Imp. Univ. 17 (1928) 1157.
[73] J.S. Kouvel, C.C. Hartelius, J. Appl. Phys. 35 (1964) 940.
[74] W. Sucksmith, J.E. Thompson, Proc. Roy. Soc. A 225 (1954) 362.
[75] C. Kittel, Introduction to Solid State Physics, sixth ed., Wiley, New York, 1986.
[76] V. Weihnacht, L. Péter, J. Tóth, J. Pádár, Z. Kerner, C.M. Schneider, I. Bakonyi, J. Electrochem. Soc. 150 (2003) C507.
[77] L. Péter, J. Pádár, E. Tóth-Kádár, Á. Cziráki, P. Sóki, L. Pogány, I. Bakonyi, Electrochim. Acta 52 (2007) 3813.
[78] B.D. Cullity, S.R. Stock, Elements of X–ray Diffraction, third ed., Prentice Hall, Upper Saddle River, New Jersey, U.S:A., 2001.
[79] J. Gubicza, X-ray Line Profile Analysis in Materials Science, IGI-Global, Hershey, PA, USA, 2014, ISBN: 978-1-4666-5852-3.
[80] J.L. Lábár, M. Adamik, B.P. Barna, Zs. Czigány, Zs. Fogarassy, Z.E. Horváth, O. Geszti, F. Misják, J. Morgiel, G. Radnóczi, G. Sáfrán, L. Székely, T. Szüts, Microscopy Microanal. 18 (2012) 406–420.
[81] R. Winand, Electrochim. Acta 39 (1994) 1091.
[82] J.W. Diny, Electrodeposition. The Materials Science of Coatings and Substrates, Noyes Publications, Park Ridge, NJ, USA, 1993.
[83] E. Gómez, S. Pané, E. Vallés, Electrochim. Acta 51 (2005) 146.
[84] A. Karimzadeh, M. Aliofkhazraei, J.C. Walsh, Surf. Coat. Technol. 372 (2019) 463.
[85] S. Spanou, E.A. Pavlatou, N. Spyrellis, Electrochim. Acta 54 (2009) 2547.
[86] I. Bakonyi, E. Tóth-Kádár, L. Pogány, Á. Cziráki, I. Gerőcs, K. Varga-Josepovits, B. Arnold, K. Wetzig, Surf. Coat. Technol. 78 (1996) 124.
[87] E. Tóth-Kádár, I. Bakonyi, L. Pogány, Á. Cziráki, Surf. Coat. Technol. 88 (1997) 57.
[88] M. Cerisier, K. Attenborough, J.P. Celis, C. Van Haesendonck, Appl. Surf. Sci. 166 (2000) 154.
[89] S. Armyanov, S. Vitkova, Surface Technol. 7 (1978) 319.
[90] S. Armyanov, Electrochim. Acta 45 (2000) 3323.
[91] M.S. Bhuiyan, B.J. Taylor, M. Paranthaman, J.R. Thompson, J.W. Sinclair, J. Mater. Sci. 43 (2008) 1644.
[92] I. Bakonyi, E. Simon, B.G. Tóth, L. Péter, L.F. Kiss, Phys. Rev. B 79 (2009), 174421.
[93] I. Bakonyi, L. Péter, Z.E. Horváth, J. Pádár, L. Pogány, G. Molnár, J. Electrochem. Soc. 155 (2008) D688.
[94] L. Seligman, M.L. Sartorelli, A.A. Pasa, W. Schwarzacher, O.I. Kasyutich, J. Magn. Magn. Mater. 226 (2001) 752.
[95] M.L. Munford, M.L. Sartorelli, L. Seligman, A.A. Pasa, J. Electrochem. Soc. 149 (2002) C274.
[96] J.M. Daughton, J. Magn. Magn. Mater. 192 (1999) 334.
[97] R.C. Munoz, C. Arenas, Appl. Phys. Rev. 4 (2017), 011102.
[98] J. Banhart, H. Ebert, A. Vernes, Phys. Rev. B 56 (1997) 10165.
[99] I. Turek, T. Záležák, J. Phys.: Conf. Series 200 (2009), 052029.
[100] H. Ebert, S. Mankovsky, K. Chadova, S. Polesya, J. Minár, D. Ködderitzsch, Phys. Rev. B 91 (2015), 165132.
[101] D. Wagenknecht, I. Turek, J. Phys.: Condens. Matter 32 (2020), 185802.
[102] D. Gall, J. Appl. Phys. 119 (2016), 085101.
[103] I. Bakonyi, Eur. Phys. J. Plus 136 (2021) 410.
[104] I. Bakonyi, V.A. Isnaini, T. Kolonits, Z. Czigány, J. Gubicza, L.K. Varga, E. Tóth-Kádár, L. Pogány, L. Péter, H. Ebert, Philos. Mag. 99 (2019) 1139.
[105] M.J. Laubitz, T. Matsumura, P.J. Kelly, Can. J. Phys. 54 (1976) 92.
[106] M.J. Laubitz, T. Matsumura, Can. J. Phys. 51 (1973) 1247.
[107] The room–temperature resistivity of fcc–Co was estimated in Ref. 92 on the basis of the high–temperature resistivity data reported for fcc–Co and hcp–Co in Ref. 106.